The allosteric modulation of Complement C5 by knob domain peptides

Alex Macpherson[1,2]*, Maisem Laabei[2], Zainab Ahdash[1], Melissa Graewert[3], James R. Birtley[1], Sarah Schulze[1], Susan Crennell[2], Sarah A. Robinson[4], Ben Holmes[1], Vladas Oleinikovas[1], Per H. Nilsson[5,6], James Snowden[1], Victoria Ellis[1], Tom Eirik Mollnes[6,7,8], Charlotte M. Deane[4], Dmitri Svergun[3], Alastair D.G. Lawson[1] and Jean van den Elsen[2,9]*

[1] UCB, Slough, UK. SL1 3WE;

[2] Department of Biology and Biochemistry, University of Bath, Bath, UK. BA2 7AX;

[3] European Molecular Biology Laboratory, Hamburg Unit, 22607 Hamburg, Germany;

[4] Department of Statistics, University of Oxford, Oxford, UK;

[5] Department of Chemistry and Biomedicine, Linnaeus University, 391 82 Kalmar, Sweden;

[6] Department of Immunology, Oslo University Hospital, University of Oslo, Oslo, Norway;

[7] Research Laboratory, Bodø Hospital, K.G. Jebsen TREC, University of Tromsø, Tromsø, Norway;

[8] Centre of Molecular Inflammation Research, Norwegian University of Science and Technology, Trondheim, Norway;

[9] Centre for Therapeutic Innovation, University of Bath, Bath, UK. BA2 7AX

*email alex.macpherson@ucb.com and bssjmhve@bath.ac.uk

To overcome limited germline combinatorial diversity, bovines have evolved a subset of antibodies with ultra-long CDRH3 regions that harbour cysteine-rich knob domains. To produce affinity-matured peptides, we previously isolated autonomous 3-6 kDa knob domains from bovine antibodies. Here, we show that binding of four knob domain peptides elicits a range of effects on the clinically validated drug target complement C5. Allosteric mechanisms predominated, with one peptide selectively inhibiting C5 cleavage by the alternative pathway C5 convertase, revealing a targetable mechanistic difference between the classical and alternative pathway C5 convertases. Taking a hybrid biophysical approach, we present C5-knob domain co-crystal structures and, by solution methods, observed allosteric effects propagating >50 Å from the binding sites. This study expands the therapeutic scope of C5, presents new inhibitors and introduces knob domains as new, low molecular weight antibody fragments, with therapeutic potential.

1   By the end of 2019, over 60 peptide drugs have received regulatory approval, with an

2   estimated 400 more in active development globally (Lau and Dunn, 2018; Lee *et al.*, 2019).

3   As a potential route to discover therapeutic peptides, we previously reported a method for

4   deriving peptides from the ultralong heavy chain complementarity determining region 3 (ul-

5   CDRH3), which are unique to a subset of bovine antibodies(Macpherson *et al.*, 2020). We

6   have shown that knob domains, a cysteine-rich mini-domain common to all ul-CDRH3, can

7   bind antigen autonomously when removed from the antibody scaffold(Macpherson *et al.*,

8   2020). This allows peptide affinity maturation to be performed *in vivo*, harnessing the cow's

9   immune system to produce peptides with complex stabilising networks of disulphide bonds.

10 For the discovery of knob domain peptides, immunisation of cattle is followed by cell sorting

11 of B-cells using fluorescently labelled antigen. A library of antigen-specific CDRH3

12 sequences is created by performing a reverse transcription polymerase chain reaction (RT

13 PCR) on the B-cell lysate, followed by a polymerase chain reaction (PCR) using primers

14 specific to the conserved framework regions which flank CDRH3(Macpherson *et al.*, 2020).

15 Upon sequencing, ul-CDRH3 are immediately evident and the knob domains can be

16 expressed recombinantly as cleavable fusion proteins(Macpherson *et al.*, 2020).

17 This method for discovery of knob domain peptides was established using Complement

18 component C5, and we reported peptides which bound C5 with affinities in the pM - low nM

19 range(Macpherson *et al.*, 2020). Herein, we use these novel peptides to probe the structural

20 and functional aspects of C5 activation.

21 C5 is the éminence grise of the complement cascade's druggable proteins, and the target of

22 effective therapies for diseases with pathogenic complement dysregulation, of which

23 paroxysmal nocturnal haemoglobinuria(Rother *et al.*, 2007) and atypical haemolytic uremic

24 syndrome(Nurnberger *et al.*, 2009) are notable examples. Six monoclonal antibodies

25 targeting C5 have reached, or are entering, clinical trials, closely followed by C5-targeting

26 immune evasion molecules(Romay-Penabad *et al.*, 2014), aptamers(Biesecker *et al.*, 1999),

27 cyclic peptides(Ricardo *et al.*, 2014), interfering RNA(Borodovsky *et al.*, 2014), and small

28 molecules(Jendza *et al.*, 2019). Currently, C5 inhibitors are being trialled for the treatment of

29 acute respiratory distress syndrome arising from SARS-CoV-2 infection(Smith *et al.*, 2020;

30 Wilkinson *et al.*, 2020; Zelek *et al.*, 2020).

31 C5 is the principal effector of the terminal portion of the complement cascade. At high local

32 C3b concentrations, arising from activation of either or both of the classical (CP) and

33 mannose binding lectin (LP) pathways, aided by the amplificatory alternative pathway (AP),

34 C5 is cleaved into two moieties with distinct biological functions. Cleavage is performed by

35   two convertases; C4bC2aC3b, formed in response to CP or MBL activation (henceforth the

36   CP C5 convertase), and C3bBbC3b, formed in response to AP activation (henceforth the AP

37   C5 convertase). Although the constitutive components of the C5 convertases differ, they are

38   thought to be mechanistically identical. Once cleaved, the C5a fragment is the most

39   proinflammatory anaphylatoxin derived from the complement cascade. When signalling

40   through C5aR1 and C5aR2, C5a is a strong chemoattractant recruiting neutrophils,

41   eosinophils, monocytes, and T lymphocytes to sites of complement activation, whereupon it

42   activates phagocytic cells, prompting degranulation. C5b meanwhile, interacts with C6,

43   recruiting C7-C9 to form the terminal C5b-9 complement complex (TCC). Once inserted into

44   a cell membrane, the TCC is referred to as the membrane attack complex, a membrane-

45   spanning pore which can lyse sensitive cells.

46   Aspects of the structural biology of C5 are well understood, due to a crystal structure of the

47   apo form(Fredslund *et al.*, 2008) and a number of co-crystal structures of C5 with various

48   modulators. By virtue of its constitutive role in the terminal pathway, C5 is a recurrent target

49   for immune evasion molecules and structures have been solved of C5 in complex with an

50   inhibitory molecule derived from *Staphylococcus aureus*, SSL-7(Laursen *et al.*, 2010), as

51   well as several structurally distinct examples from ticks: OmCI(Jore *et al.*, 2016), RaCI(Jore

52   *et al.*, 2016) and Cirp-T(Reichhardt *et al.*, 2020). Additionally, the structures of C5 with the

53   inhibitory monoclonal antibody (mAb) eculizumab(Schatz-Jakobsen *et al.*, 2016), of C5 with

54   a small molecule inhibitor(Jendza *et al.*, 2019), and of C5 with the complement depleting

55   agent Cobra Venom Factor (CVF)(Laursen *et al.*, 2011), have all been determined.

56   Here, we probe C5 with knob domain peptides and explore the molecular processes which

57   underpin allosteric modulation of this important drug target. This study is the first to

58   investigate the molecular mechanisms and pharmacology of this recently isolated class of

59   peptide.

60   **Results**

61   **Functional characterisation of anti-C5 bovine knob domain peptides.** Complement

62   activation assays were performed, using two ELISA kits which measured CP and AP

63   activation in human serum, through C5b neo-epitope formation and C5a release. Orthogonal

64   ELISA assays, which measured C3b and C9 deposition, were also developed (Figure 1, a-b).

65   We tested four knob domain peptides: K8, K57, K92 and K149, which have been previously

66   reported to display tight binding to C5(Macpherson *et al.*, 2020).

67　By ELISA, K57 was a potent and fully efficacious inhibitor of C5 activation, preventing

68　release of C5a, and deposition of C5b and C9. As expected, there was no effect on C3b,

69　which is upstream of C5. In contrast, K149 was a high affinity silent binder with no

70　discernible effect on C5a release, formation of C5b neo-epitope or C9 deposition, even at

71　peptide concentrations in excess of 100 x K_D (Supplementary Section 1).

72　K8 and K92 exerted more nuanced allosteric effects on C5. By ELISA, K92 partially

73　prevented C5 activation by the AP but, intriguingly, no effect was observed in assays where

74　the AP component was not isolated, suggesting K92 selectively inhibits C5 activation by the

75　AP C5 convertase. Partial antagonists, where the degree of inhibition for the asymptotic

76　concentrations of a dose response curve (E_{max}) is below 100 %, are an impossible mode of

77　pharmacology for orthosteric antagonists(Klein, Vinson and Niswender, 2013) and we

78　therefore propose that K92 operates by a non-steric mechanism. K8 was also demonstrably

79　allosteric, partially inhibiting both the AP and CP in ELISA experiments. For K8 and K92, no

80　effect on C3b deposition was detected.

81　When tested in CP and AP haemolysis assays, K57 was a potent and fully efficacious

82　inhibitor of complement mediated cell lysis. Consistent with the ELISA data, K92 was active

83　solely in the AP-driven haemolysis assay, achieving E_{max} values of 30-40 %; while K8 was

84　efficacious in the CP assay but did not show activity in the AP assay below 10 µM,

85　potentially a consequence of the increased serum concentration and stringency of the

86　haemolysis endpoint.

87　**Crystal structure of the C5-K8 peptide complex.** To elucidate the structural basis for the

88　allosteric modulation of C5, we determined the crystal structure of the C5-K8 complex at a

89　resolution of 2.3 Å (Supplementary 2.1 shows data collection and structure refinement

90　statistics). The structure of the C5-K8 complex shows the K8 peptide binding to a previously

91　unrecognised regulatory site on C5; the macroglobulin (MG) 8 domain of the α-chain (Figure

92　2a-b).　K8 adopts a cysteine knot configuration, where a flattened 3-strand β-sheet topology

93　is constrained by three disulphide bonds (Figure 3 and Supplementary 2.5). Analysis of the

94　K8-C5 complex with the macromolecular interfaces analysis tool PDBePISA(Krissinel and

95　Henrick, 2007), reveals a large interaction surface (comprising 1639Å^2; 849Å^2 contributed by

96　K8 and 790Å^2 by C5), comparable to those seen in Fab-antigen complexes, stabilised by an

97　extensive network of 18 hydrogen bonds between K8 and the MG8 domain (Supplementary

98　2.6), dominated by arginine residues R23$_{K8}$, R32$_{K8}$ and R45$_{K8}$. The extensive H-bond

99   network is further bolstered by ionic interactions, between R32$_{K8}$ and D1471$_{C5}$ (C5

100   numbering based on mature sequence), D25$_{K8}$ and K1409$_{C5}$, and H36$_{K8}$ and D1382$_{C5}$

101   (Supplementary 2.7). The opposing face of K8 was fortuitously stabilised by a substantial,

102   1275.1 Å^2, crystal contact with the C5d domain of a symmetry-related C5 molecule,

103   (Supplementary 2.2), ensuring clear electron density and clearly enunciating the disulphide

104   bond arrangement and backbone and side chains interactions. A mFo-DFc simulated

105   annealing omit map of the C5-K8 complex is displayed in Supplementary 2.4, showing clear

106   electron density for the K8 peptide. Despite the overall resolution of the dataset comparing

107   favourably with other C5 structures in the PDB(Schatz-Jakobsen *et al.*, 2016; Laursen *et al.*,

108   2010; Jore *et al.*, 2016; Fredslund *et al.*, 2008), density for the C345C domain was largely

109   absent, due to this flexible domain occupying a solvent channel.

110   **Crystal structure of the C5-K92 complex**. We also present a crystal structure of the C5-

111   K92 complex at a resolution of 2.75 Å (Supplementary 2.1 shows data collection and

112   structure refinement statistics). Continuous electron density for the flexible C345C domain of

113   C5 was observed, due to it being stabilised in an upward pose by crystal contacts, akin to the

114   C5-RaCI-OmCI ternary complex structures (Protein Data Bank [PDB] accession codes:

115   5HCC, 5HCD and 5HCE(Jore *et al.*, 2016)). Despite being higher affinity than K8, density

116   for K92 was not as well defined and so, to aid model building, we used mass spectrometry to

117   perform a disulphide mapping experiment. The disulphide map of K92 identified formation

118   of disulphide bonds between C9$_{K92}$ and C23$_{K92}$ and between C2$_{K92}$ and C18$_{K92}$

119   (Supplementary 2.8), enabling completion of the model. A mFo-DFc simulated annealing

120   omit map of the C5-K92 complex is displayed in Supplementary 2.4, showing clear electron

121   density for the peptide.

122   Similar to K8, K92 adopts a 3-strand β-sheet topology (Figure 2 c-d and Supplementary 2.9)

123   but with only two disulphide bonds. With shorter β-strands and longer connecting loop

124   regions, K92 exhibits a more compact, globular arrangement (Figure 3b). Two extended loop

125   regions interact with C5, including an α-helix containing loop between β-strands 1 and 2,

126   occupying a cleft between the MG1 and MG5 domains of the β-chain of C5. The 1365Å^2

127   interaction surface is sustained via a sparse set of eight H-bonds (Supplementary 2.10). An

128   elegant series of π-π and aliphatic–aromatic stacking interactions spans K92, encompassing:

129   F26$_{K92}$, H25$_{K92}$, W21$_{K92}$, W6$_{K92}$ and P3$_{K92}$, (Supplementary 2.11). From within this

130   hydrophobic patch, important H-bonds occur between H25$_{K92}$ and the backbone carbonyls of

131   N77$_{C5}$ and N81$_{C5}$ on the MG1 domain.

132   The epitope for K92 is entirely contained within the binding interface of a previously

133   reported immune evasion molecule, the 23 kDa SSL7 protein from *Staphylococcus aureus*.

134   The C5-SSL7 crystal structure reveals the core of that interaction to be a series of five H-

135   bonds between SSL7 and a region of β-sheet on the MG5 domain, spanning $H511_{C5}$-$E516_{C5}$

136   (Laursen *et al.*, 2010). Our structure shows that K92 also interacts with this area, inducing a re-

137   orientation of the sidechain of $H511_{C5}$ and forming a backbone H-bond with $F510_{C5}$, but

138   critically also makes interactions with the MG1 domain, effectively cross-linking the MG1

139   and MG5 domains. These changes beget different allosteric effects; SSL7, either in isolation

140   or in complex with its second ligand IgA, is full, or occasional partial, antagonist of both the

141   AP and CP(Bestebroer *et al.*, 2010; Laursen *et al.*, 2010), while K92 is a selective partial

142   antagonist of the AP.

143   **The multi-purpose role of disulphide bonds.** In the near absence of secondary structure,

144   disulphide bonds are sources of stability for both peptides. For K92, both the backbone amide

145   and carbonyl of $C23_{K92}$ participate in H-bonds with the sidechain of $S82_{C5}$, with close

146   proximity to the electron dense disulphide bond lowering the conformational and desolvation

147   entropy of these polar interactions. Within the knob domain paratopes, disulphide bonds also

148   participate in sulphur-π interactions. For K8, an interchain sulphur-π stack between the

149     $C26_{K8}$-$C40_{K8}$ disulphide bond and the aromatic of $Y1378_{C5}$, elegantly positions the hydroxyl

150   group of $Y1378_{C5}$ to make a H-bond with $D24_{K8}$. While for K92, an intra-chain sulphur-π

151   stack between the $C9_{K92}$-$C23_{K92}$ disulphide bond and the aromatic of $Y14_{K92}$ was used to

152   orientate $Y14_{K92}$, such that its hydroxyl group could participate in an interchain H- bond with

153     $N38_{C5}$.

154   Both K8 and K92 have prominent non-polar surface features (Figure 3). In addition to three

155   disulphide bonds, K8 has several aromatic residues, $F7_{K8}$, $W9_{K8}$, $Y11_{K8}$, $F20_{K8}$, $W26_{K8}$,

156     $Y29_{K8}$, $Y38_{K8}$, $F40_{K8}$, $Y50_{K8}$ and $F51_{K8}$, most of which occupy the opposing face and do not

157   participate in the paratope. Hydrophobicity may be part of a specific strategy to maximise

158   free enthalpy from the limited set of polar interactions. So, to evaluate bond enthalpy, we

159   performed binding pose metadynamics(Clark *et al.*, 2016), an analysis typically employed to

160   computationally evaluate the binding stability of chemical ligands(Fusani *et al.*, 2020). This

161   *in silico* analysis suggested that both K8 and K92's binding poses were exceptionally stable,

162   with the interface maintaining the key interactions in spite of applied force (Supplementary

163   2.6 and 2.7). This, in conjunction with earlier kinetic studies(Macpherson *et al.*, 2020),

164   highlights quality of the interactions made by both knob domains.

6

165 **Comparison to known antibody paratopes.** Although antibody derived, K8 and K92 are

166 structurally unique variable regions. We compared the K8 and K92 knob domains to a non-

167 redundant set of 924 non-identical sequences of paired antibody-protein antigen structures

168 from SAbDab(Dunbar *et al.*, 2014). Paratopes were defined as any antibody residues within

169 4.5 Å of the antigen in the structure. The paratopes of K8 and K92 contain 18 and 10

170 residues, respectively, which are within the typical range of antibody paratope sizes

171 (Supplementary 2.14). Given this similarity in size, we searched for structurally and

172 physicochemically similar antibody paratopes from the 924 antibody complexes but no

173 similar paratope sites were found(Wong *et al.*, 2020). While the limited examples preclude

174 firm conclusions, this lack of similarity could be due either to the unusual fold of the knob

175 domains or to differences in paratope amino acid composition.

176 In terms of residue usage, one difference in paratope composition that is potentially universal

177 is the presence of cysteine in the knob domains (Supplementary 2.15) which is uncommon in

178 most antibody paratopes apart from broadly neutralising antibodies(Hutchinson *et al.*, 2019).

179 Using Arpeggio(Jubb, 2015) to identify inter- (antigen contacting) and intra-paratope

180 interactions revealed that on average, antibodies have 16 intra-paratope and 17 inter-paratope

181 interactions; K8 is very close to this, with 15 intra-paratope and 17 inter-paratope

182 interactions, whereas K92 paratope has fewer, with 9 intra-paratope and 10 inter-paratope

183 interactions. A bovine Fab with an ul-CDRH3 was recently crystallised in complex with

184 antigen, in this case a soluble portion of the HIV envelope(Stanfield *et al.*, 2020). While the

185 low resolution of the crystal structure hindered analysis, a casual inspection of the paratope

186 suggests 10 intra-paratope and 10 inter-paratope interactions are sustained by the knob

187 domain, comparable to K92.

188 A search for structurally homologous proteins, using the DALI protein structure comparison

189 server(Holm, 2020), did not find any 3-D structures similar to K8 or K92, including amongst

190 the 14 structures of bovine Fabs with ul-CDRH3 in the PDB, potentially as a consequence of

191 knob domains being shaped by their antigen.

192 **Solution techniques reveal allosteric networks.** To contextualise our functional and

193 structural data, we analysed the C5-knob domain complexes by two solution biophysical

194 techniques – small angle X-ray scattering (SAXS) and hydrogen deuterium exchange mass

195 spectrometry (HDX-MS).

7

196   SEC-SAXS, where size exclusion chromatography (SEC) immediately precedes the solution

197   X-ray experiment ensuring a monodispersed sample, was performed in concert with SEC-

198   MALLS (multi angle laser light scattering). Data were collected for C5 and the C5-K8, C5-

199   K57, C5-K92 and C5-K149 complexes. (Figure 4a-c). SEC-MALLS confirmed that the

200   increases in molecular weight of the complexes were consistent throughout the elution peaks

201   (Supplementary 3.1 and 3.2). Interestingly, while SEC-SAXS elution profiles gave stable

202   estimates of the radius of gyration (R_G) across the tip of the peak, frames from the descending

203   elution peaks show lower R_G values, suggesting either the presence of unbound C5 in the

204   sample, which our SEC-MALLS data would preclude, or two distinguishable conformational

205   states.

206   Frames corresponding to the tip of the peak were averaged and submitted for full SAXS

207   analysis. For the complexes, the scattering curves showed slight increases in both the R_G and

208   solute volume (Supplementary 3.1), with the C5-K8 complex showing the largest change and

209   C5-K149 the smallest change, corresponding with the absence of function and suggesting

210   K149 binds peripherally to a conformation closely resembling apo C5. For K92 and K57, the

211   discrepancies observed in the mid s range indicate an overall change in flexibility of C5 upon

212   binding of these peptides, and this tuning of dynamics may contribute to their mechanism.

213   Consistent with earlier observations(Fredslund *et al.*, 2008), comparison of the apo C5

214   experimental data with the theoretical scattering curve revealed discrepancies in the lowest

215   angle range, indicating C5 adopts a more elongated conformation in solution than the crystal

216   structure would suggest (Supplementary 3.3). To better approximate C5 in solution we

217   performed a normal mode model analysis (NMA) using SREFLEX(Panjkovich and Svergun,

218   2016) and found that elongation of the C5 model improved the χ^2 from >13 to 1.55. The fit of

219   the C5-K92 complex was also markedly improved by the NMA (Supplementary 3.3),

220   whereby elongation and incorporation of the peptide improved the model from an initial χ^2 of

221   >20, to 2.5 (with an overall root-mean-square [RMS] of 3.8 in both cases).

222   When using the C5-K8 co-crystal structure for fitting of the C5-K8 SAXS data, the absence

223   of the C345C domain was problematic. The generation of a hybrid model where the C345C

224   domain was reinstated produced a poor fit ($\chi^2 = 75$). Despite significant remodelling of

225   C345C, we were unable to describe the solution structure in more detail. As the data were

226   collected in SEC mode, it is unlikely that increases in R_G values and volume are due to

227   oligomerisation and instead may suggest increased flexibility around the C345C linker. The

8

228   absence of clear electron density for the C345C domain in the crystal structure may be a

229   consequence of K8 inducing additional flexibility to this region, which again could contribute

230   to the efficacy of the peptide.

231   The discrepancies between the crystal structures and the solution scattering data indicate that

232   while permitting elucidation of the molecular interaction of the epitopes, the constraints of

233   the crystal lattice may impede the detection of more subtle, global changes, leading to

234   underestimation of the conformational changes induced by the peptide.

235   To further explore such effects in solution, we used HDX-MS to provide molecular level

236   information on local protein structure and dynamics. HDX-MS measures the exchange of

237   backbone amide hydrogen to deuterium in the solvent, with the rate of HDX determined by

238   solvent accessibility, protein flexibility, and hydrogen bonding. To interpret the impact of

239   peptide binding on C5 structural dynamics, we performed differential HDX (ΔHDX)

240   analysis, comparing C5-knob domain complexes to apo C5, where shielding of C5 residues

241   through participation in a binding interface will prevent deuteration, while conformational

242   changes may increase or decrease deuterium uptake, in relation to the degree of solvent

243   exposure.

244   For C5-K8, the sole protected region of C5 corresponded to the epitope on the MG8 domain

245   ($L1380_{C5}$-$E1387_{C5}$), although the interface was not entirely defined (Figure 5a). Additional

246   conformational changes were observed in the neighbouring C5d domain which becomes

247   more solvent exposed, suggesting K8 is affecting the dynamics of this domain.

248   For the C5-K92 complex, consistent with the crystal structure, there was protection of the C5

249   residues located in the epitope between the MG1 and MG5 domains ($H70_{C5}$-$L85_{C5}$), shown in

250   Figure 5c. There were also effects distal to the K92 binding site, notably in C5d ($I1169_{C5}$-

251    $F1227_{C5}$) and neighbouring CUB domain ($L1303_{C5}$-$L1346_{C5}$), indicating a K92-induced

252   conformational change. Interestingly, the allosteric network can be visualised by changes in

253   solvent exposure which propagate from the K92 epitope through MG2 domain ($L126_{C5}$-

254    $V145_{C5}$) and into the C5d and CUB domains. For the C5-K57 complex, the absence of a co-

255   crystal structure meant we had no prior knowledge of the K57 epitope. However, clear

256   protection was observed in the MG5 domain, immediately adjacent to the K92 epitope

257   ($N483_{C5}$-$L540_{C5}$), with sparse areas of increased solvent exposure located in the MG6

258   ($Q572_{C5}$-$L590_{C5}$), MG8 ($L1379_{C5}$-$A1388_{C5}$) and C5d ($K1048_{C5}$-$Y1064_{C5}$) domains. A single

259   protected peptide was also present in the CUB domain (G951$_{C5}$-L967$_{C5}$), suggesting the K57

260   epitope may be on either the MG5 or CUB domains.

261   The helical C5d domain is the target of two immune evasion molecules which have evolved

262   in ticks, OmCI and RaCI, both of which inhibit C5 by crosslinking C5d to neighbouring

263   domains(Jore *et al.*, 2016). Additionally, it has been shown that polyclonal antibodies raised

264   against C5d inhibit binding of C5 to C3b(DiScipio, 1992). The binding site of OmCI is

265   contained within the CUB and C5d domains, with only a single, non-bonded interaction to

266   the C345C domain visible in the crystal structure(Jore *et al.*, 2016), which appears mediated

267   by crystal contacts. This may suggest that K92 and K8 achieve efficacy in a manner similar

268   to OmCI by modulating the C5d and CUB domains, but, in the case of K92, at a range of

269   over 50 Å. Such remote effects are not unprecedented; allosteric structural changes can be

270   propagated at over 150 Å in response to drug binding(Haselbach *et al.*, 2017). SSL7, which

271   similarly binds the MG1-MG5 domains is also a partial antagonist, suggesting it too has an

272   allosteric mechanism but not one which is selective for the AP.

273   There was little protection or deprotection of proteolytic fragments of the C5a domain in any

274   of the complexes, we therefore propose that the knob domain peptides do not act by inducing

275   conformational changes which shield the scissile arginine bond. The binding of K8, however,

276   may induce some flexibility of C5a, as only sparse continuous electron density was observed

277   for the N-terminal the linker extending from MG6 to this domain in the crystal structure.

278   Taken in the context of the other changes, notably in the C5d and CUB domains, it is more

279   probable that they affect more global changes in C5 which lower the affinity for C3b or the

280   C5 convertases.

281   **Experimental validation of cooperativity** We hypothesised that these conformational

282   changes may manifest as cooperativity between the different knob domain epitopes. To test

283   this, we performed a SPR cross blocking-experiment where, using a Biacore 8K, we saturated

284   a C5 coated sensor chip with two 20 µM injections of knob domain peptide before injecting a

285   different peptide at 20 µM to assess its capacity to bind. Saturation of C5 with the non-

286   functional K149 did not prevent subsequent binding of K8, K57 or K92 (Figure 6d),

287   suggesting K149 does not share an epitope with the other ligands, nor does it significantly

288   perturb C5 such that the other binding sites are affected.

289   We detected negative cooperativity between the distal binding sites of K8 and K92, where,

290   somewhat surprisingly, saturation of C5 with K8 entirely prevented binding of K92. Given

291   the degree of separation between the K8 and K92 epitopes, in excess of 50 Å, and the

292   conformational changes detected by HDX-MS analysis, we propose a non-steric mechanism

293   whereby competition between K8 and K92 arises by negative cooperativity between the two

294   distal epitopes. Correspondingly, when the order of addition was changed and C5 was

295   saturated with K92, K8 was still able to bind, albeit to a lesser degree (Figure 6b). Saturation

296   of C5 with K8 also entirely eliminated binding of K57, with a similar order of addition effect,

297   whereby K8 could still partially bind to the C5-K57 complex (Figure 6a).

298   When C5 was saturated with K92 or K57 only very small amounts of subsequent binding of

299   either peptide were observed by SPR (Figure 6c). Suggesting that the epitopes do not overlap

300   but that considerable negative cooperativity exists. To further home in on the K57 binding

301   site we measured binding to C5b in a SPR single-cycle kinetics experiment (Supplementary

302   5.1). Upon cleavage of C5a the remaining domains of the α-chain undergo a substantial

303   conformational change, mediated by rearrangement of the MG8, CUB and C5d

304   domains(Hadders *et al.*, 2012; Aleshin *et al.*, 2012). By SPR, K8 did not bind C5b, a likely

305   consequence of conformational rearrangement of the CUB domain. However, K57, K92 and

306   K149 all bound C5b with equal affinity to C5 (Supplementary 5.2). As the CUB domain is

307   significantly altered in C5b, this increases the likelihood that, of the two protected regions

308   identified by HDX-MS, the K57 epitope is on the MG5 domain.

309   By HDX-MS and SPR, we saw considerable long-range effects with all knob domains, with

310   the exception of non-functional K149. We therefore suggest that knob domain peptides may

311   be well suited to the allosteric modulation of proteins and that C5 may be particularly

312   susceptible to modulation by such approaches.

Discussion

313   We present knob domain peptides as novel therapeutic molecules, which rely on the bovine

314   immune system to achieve high affinity binding through optimisation of amino acid

315   composition, 3-D structure and disulphide bond network. Knob domains have only been

316   recently isolated as a practicable antibody fragment(Macpherson *et al.*, 2020) and therefore

317   structural information will greatly aid their development as therapeutics.

318   Due to the apparent structural homology of knob domains with certain venomous peptides, of

319   which conotoxins and spider venoms are examples; it has been proposed that the knob

320   domains of ul-CDRH3 might be similarly predisposed to target the concave epitopes of ion

321   channels. Likewise, structural homology with defensin peptides has garnered hypotheses

322   regarding an improved ability to bind viral capsid coats. Indeed, bovine antibodies with ul-

323   CDRH3 have been raised against the viral capsid of HIV with exceptional efficiency, given

324   the challenging nature of the antigen(Sok *et al.*, 2017; Stanfield *et al.*, 2020). However, the

325   study presented here shows that, in the case of C5, concave epitopes are not the knob

326   domain's sole preserve. Notably, the MG8 domain epitope of K8 offers a planar

327   pharmacophore and, while the K92 epitope is more undulating, casual inspection of the C5

328   structure reveals numerous deeper cavities available.

329   We note that the structural architecture of the knob domains varies for the epitope. Their

330   immune derivation means that, unlike cysteine-rich peptides derived from other natural

331   sources, such as venoms, the bovine immune system can be used to define specificity for any

332   antigen. Comparative structural analysis suggests knob domain paratopes are differentiated

333   from conventional antibodies, offering a different binding architecture to the ubiquitous VHH

334   antibody fragment. While firm conclusions are hampered by limited examples, the number of

335   interactions does not seem dissimilar from a mAb, which might be beneficial for tackling

336   high affinity protein-protein interactions.

337   Knob domains offer hydrophobic paratopes, from which binding affinities broadly

338   comparable to a conventional mAb can be obtained. The latent hydrophobicity is a likely

339   consequence of germline priming for cysteine mutations which means the conserved IGDH8-

340   2 D- gene segment, which encodes the knob domain and majority of the stalk, contains an

341   astonishing 15 glycine and 17 tyrosine residues, each of which can be mutated to cysteine

342   with a single base pair change. We propose that hydrophobicity may be a strategy to

343   minimise desolvation entropy and thereby maximise the value of a H-bond network, enabling

344   the most ligand-efficient, antibody-derived binding domain described to date.

345   Our structures demonstrate that the importance of the network of disulphide bonds goes

346   beyond a stabilising role. An apparent paucity of secondary structure would suggest that

347   stabilisation of the domain is indeed critical, but disulphide bonds are also a source of

348   electron density for the paratope. We show that this electron density mediates sulphur-π

349   interactions between the disulphide bond and nearby aromatic residues mediating intra- and

350   inter-chain interactions. Finally, the disulphide bonds contribute even more hydrophobicity

351   to the paratope which can improve the free enthalpy of local polar interactions. For example,

352   the backbone amide and carbonyl of C23$_{K92}$ form interchain H-bonds with C5, capitalising on

12

353 the stability and proximal electron density of the disulphide bond to lower conformational

354 and desolvation entropy.

355 Functional characterisation at the level of individual complement pathways identified K57 as

356 a novel C5 inhibitor, which is a fully efficacious inhibitor of the terminal pathway in response

357 to both CP and AP activation, and a potential therapeutic candidate for complement mediated

358 disorders. Additionally, the discovery of K149 as a 'silent binder' of C5 may be of

359 considerable value as a non-inhibitory reagent for the detection of native C5.

360 This study used X-ray crystallography in concert with solution biophysics methods to

361 elaborate the mechanisms underpinning allosteric inhibition of proteins. With the caveat of

362 small sample size, half of the knob domains exemplified in this study were allosteric. K92

363 achieved selective inhibition of the alternative pathway through a non-competitive

364 mechanism. To our knowledge, this is the first reported example of complement pathway

365 specific inhibition through C5 and the first experimental evidence reported for mechanistic

366 differences between the AP and CP C5 convertases. This suggests an expanded therapeutic

367 scope for C5, whereby tuning of the conformational ensemble with allosteric compounds can

368 bias activation to leave certain complement pathways intact. Complete inhibition of the

369 terminal pathway has been shown to increase the susceptibility of eculizumab patients to

370 *Neisseria meningitidis* infections(McNamara *et al.*, 2017). Selective inhibition of C5-

371 cleavage by the AP C5-convertase, and not the CP C5-convertase, may partially preserve

372 serum bactericidal activity thereby lowering the risk of meningococcal disease.

373 While we cannot definitively explain why K92 was selective for the AP, through HDX-MS,

374 we detected changes in the distal CUB and C5d domains. As the mechanism of K92 is non-

375 competitive which precludes a steric mechanism, efficacy might be achieved through

376 modulation of the CUB and C5d domains, in a manner similar to the immune evasion

377 molecule OmCI. SAXS analysis also suggests that K8, K57 and K92 increase the flexibility

378 of C5 and effects on dynamics may be a contributing factor in realising efficacy. This was

379 most pronounced for K8 which appears to substantially affect the conformational sampling of

380 C345C.

381 We also saw an unexpected degree of negative cooperativity between the different knob

382 domains, suggesting that all the functional knob domains perturb the conformational state of

383 C5 such that changes are induced in different regions. K57, with an E_{max} of 100 % for both

384 pathways, was not demonstrably allosteric but still showed cooperativity with other

13

385   functional knob domains, suggesting it stabilises a conformation of C5 that is less

386   energetically favourable for binding of the other ligands. In HDX-MS experiments, K57

387   induces changes which span the length of C5, in a similar manner to K92, but the nature of

388   the changes, and route of travel, are distinct to each ligand.

389   Our observations with K92 suggest that further work may be required to elucidate the

390   mechanism of action of another binder of the MG1 and MG5 domains, SSL7. Given that

391   SSL7 can be a partial inhibitor(Laursen *et al.*, 2010), even with co-binding of IgA, this

392   precludes a steric mechanism and invites biophysical studies in solution. Additionally,

393   another tick-derived inhibitor, Cirp-T, was also recently reported as predominantly binding to

394   the MG4 domain, with an orthosteric mechanism of action attributed. However, we note that

395   published data only showed an E_{max} of < 90 % in AP driven assays(Reichhardt *et al.*, 2020),

396   indicating it is an allosteric C5 inhibitor for the AP, and potentially also the CP, C5

397   convertase, which may merit further investigation. This study highlights the importance of

398   orthogonal biophysical techniques for the accurate interpretation of crystal structures. Taking

399   a solely crystallographic approach, the constraints of the crystal lattice would have masked

400   many of the distal effects that we observed.

401   This study is the first application of knob domain peptides and reveals an unexpectedly high

402   incidence of allosteric modulators of complement C5. It is entirely possible that C5 could be

403   particularly susceptible to allosteric modulation, or that by combining solution biophysics

404   methods we may have observed effects that are typically missed. This study introduces knob

405   domain peptides as a new peptide modality with unexplored therapeutic potential for the

406   modulation of proteins and protein-protein interactions.

407   **Methods**

408   **Complement proteins.** Human C5 was affinity purified using an E141A, H164A OmCI

409   column(Macpherson *et al.*, 2018). Briefly, human serum (TCS biosciences) was diluted 1:1

410   (v/v) with PBS, 20 mM EDTA and applied to a 5 mL Hi-Trap NHS column (GE Healthcare),

411   which contained 20 mg of E141A H164A OmCI protein, at a rate of 1 mL/minute. The

412   column was washed with 5x column volumes (CV) of PBS, C5 was then eluted using 2 M

413    $MgCl_2$ and immediately dialysed into PBS. C5b was prepared from human C5 by incubating

414   C5 with CVF, factor B and factor D, at a 1:10 molar ratio, as previously described(Jore *et al.*,

415   2016). C5a was removed using a spin column with 30 kDa cut-off (Thermo Fisher).

416   **Knob domain peptide production** Knob domain peptides were expressed fused to the

417   CDRH3 of the PGT-121 Fab, as previously described(Macpherson *et al.*, 2020). Plasmid

418   DNA for each construct was amplified using QIAGEN Plasmid Plus Giga Kits. Expi293F

419   cultures were transfected with Expifectamine 293 Transfection kits (Invitrogen), as per the

420   manufacturer's instructions. The cells were cultured for four days, and supernatants harvested

421   by centrifuged at 4000 rpm for one hour. Harvested supernatants were applied to a Hi-Trap

422   Nickel excel columns (GE Healthcare) using an Akta pure (GE Healthcare). Cell supernatants

423   were loaded at 2.5 mL/minute, followed by a wash of 7x CV of PBS, 0.5 M NaCl. A second

424   wash with 7x CV of Buffer A (0.5 M NaCl, 0.02 M Imidazole, PBS pH 7.3) was performed

425   and samples were eluted by isocratic elution with 10x CV of Buffer B (0.5 M NaCl, 0.25 M

426   Imidazole, PBS (pH 7.3). Post elution, the protein containing fractions were pooled and

427   buffer exchanged into PBS, using dialysis cassettes (Thermo Fisher).

428   For isolation of the knob domain peptide, PGT-121 Fab-knob peptide fusion proteins were

429   incubated with tobacco etch virus (TEV) protease, at a ratio of 100:1 (*w/w*), for a minimum of

430   2 hours at room temperature. Peptides were purified using a Waters UV-directed

431   FractionLynx system with a Waters XBridge Protein BEH C4 OBD Prep Column (300 Å, 5

432   µm, 19 mm x 100 mm). An aqueous solvent of water, 0.1 % trifluoroacetic acid (TFA) and an

433   organic solvent of 100 % MeCN was used. The column was run at 20 mL/min at 40 ºC with a

434   gradient of 5-50 % organic solvent, over 11 minutes. Fractions containing knob peptide were

435   pooled and lyophilised using a Labconco Freezone freeze drier.

436   **Complement activation assays**. For the C3 and C9 ELISAs, microtiter plates (MaxiSorp;

437   Nunc) were incubated overnight at 4°C with 50 µL of a solution of in 75 mM sodium

438   carbonate (pH 9.6) containing either: 2.5 µg/ml aggregated human IgG (Sigma-Aldrich) for

439   CP, or 20 µg/ml zymosan (Sigma-Aldrich) for AP. As a negative control, wells were coated

440   with 1 % (w/v) BSA/PBS. Microtiter plates were washed four times with 250 µL of wash

441   buffer (50 mM Tris-HCl, 150 mM NaCl and 0.1 % Tween 20 (pH 8) between each step of the

442   procedure. Wells were blocked using 250 µL of 1 % (*w/v*) BSA/PBS for 2 hours at room

443   temperature. Normal human serum was diluted in either gelatin veronal buffer with calcium

444   and magnesium (GVB^{++}:0.1 % gelatin, 5 mM Veronal buffer, 145 mM NaCl, 0.025 % NaN$_3$,

445   0.15 mM calcium chloride, 1 mM magnesium chloride, pH 7.3; for CP) or Mg-EGTA (2.5

446   mM veronal buffer [pH 7.3] containing 70 mM of NaCl, 140 mM of glucose, 0.1 % gelatin, 7

447   mM of MgCl2, and 10 mM of EGTA; for AP). Serum was used at a concentration of 1 % in

448   CP or 5 % in AP and was mixed with serially diluted concentrations of peptides (16 µM –

15

449   15.6 nM) in GVB^{++} or Mg-EGTA buffer, and preincubated on ice for 30 minutes. Peptide-

450   serum solutions were then incubated in the wells of microtiter plates for 35 minutes for CP

451   assays (both C3b and C9 detection) or 35 min for AP (C3b) or 60 min for AP (C9), at 37 °C.

452   Complement activation was assessed through detection of deposited complement activation

453   factors using specific antibodies against C3b (rat anti-human C3d, Hycult; HM2198) and C9

454   (goat anti-human C9, CompTech; A226), at a 1:1000 dilution. Bound primary antibodies

455   were detected with HRP-conjugated goat anti-rat (Abcam; ab97057) or rabbit anti-goat

456   (Dako; P0449) secondary antibodies, at a 1:1000 dilution. Bound HRP-conjugated antibodies

457   were detected using TMB One solution (Eco-TEK) with absorbance measured at 450 nm.

458   For the C5b ELISA, assays were run using the CP and AP Complement functional ELISA

459   kits (SVAR). For sample preparation: serum was diluted as per the respective protocol for the

460   CP and AP assays. Serial dilutions of peptides were prepared and allowed to incubate with

461   serum for 15 minutes at room temperature, prior to plating.

462   For the C5a ELISA, assays were run using the Complement C5a Human ELISA Kit

463   (Invitrogen). For sample preparation: at the end of the 37 °C incubation of the serum/peptide

464   samples on the C5b ELISA assay plate, 50 µL of the diluted, activated serum was transferred

465   to a C5a ELISA assay plate containing 50 µL/well of Assay Buffer. All subsequent

466   experimental steps were performed as described in the protocol.

467   **Haemolysis assays.** GVB^{++} or Mg EGTA buffers, which had been supplemented with 2.5%

468   glucose (*w/v*), were used for the CP and AP assays, respectively. For the AP, 150 µL of rabbit

469   erythrocytes (TCS Biosciences) were washed twice, by addition of 1 mL of buffer and

470   centrifugation at 800 xg for 1 minute, and finally resuspended in 500 µL of buffer. For the

471   CP, 150 µL sheep erythrocytes (TCS Biosciences) were washed twice with 1 mL of buffer

472   and sensitised with a 1/1000 dilution of rabbit anti- sheep red blood cell stroma antibody

473   (Sigma; S1389). After a 30 °C / 30 minutes incubation, with shaking, the cells were re-

474   washed and resuspended with 500 µL of buffer. Serial dilutions of peptide were prepared in

475   the respective buffers and normal human serum was added at 1% for the CP and 4.5% for the

476   AP (corresponding to CH50 of the serum). 90 µL of peptide-serum mixtures were plated into

477   a V-bottom 96-well microtiter plate (Corning) and 10 µL of erythrocytes were added. Plates

478   were incubated for 30 minutes at 37 °C, with shaking. Finally, 50 µL of buffer was added, the

479   plates centrifuged at 800 xg, and 80 µL of supernatant was transferred to an ELISA plate

480   (Nunc) and absorbance measured at 405 nm.

16

481 **Crystallography and structure determination.** 6.1 mg/ml C5 (20 mM Tris-HCl, 75 mM

482 NaCl, pH 7.35) was mixed at a 1:1 molar ratio with either the K8 or K92 peptides.

483 Crystallisation trials were initiated by the vapor-diffusion method at 18 °C with a 1:1 mixture

484 of mother liquor (*v/v*). C5-K8 crystals were grown in a mother liquor of 0.1 M ADA, 14 %

485 ethanol (*v/v*), pH 6.0. For C5-K92 crystals, the mother liquor was 0.1 M bicine/Trizma (pH

486 8.5), 10 % (*w/v*) PEG 8000, 20 % (*v/v*) ethylene glycol, 30 mM sodium fluoride, 30 mM

487 sodium bromide, 30 mM sodium iodide(Gorrec, 2009). Prior to flash freezing in liquid

488 nitrogen, C5-K8 crystals were cryoprotected in mother liquor with 30 % MPD (*v/v*). C5-K92

489 crystals were frozen without additional cryoprotection.

490 Data were collected at the Diamond Light Source (Harwell, UK), on beamline I03, at a

491 wavelength of 0.9762 Å. The C5-K8 structure was solved using the automated molecular

492 replacement pipeline Balbes(Long *et al.*, 2008) using the apo C5 structure (PDB accession

493 code: 3CU7), minus the C345c domain. The C5-K8 complex crystallised in space group

494 $P2_12_12_1$ with 1 molecule in the asymmetric unit. A backbone model of the K8 peptide was

495 produced using ARP-wARP(Langer *et al.*, 2008) which informed manual model building in

496 Coot(Emsley *et al.*, 2010), within the CCP4 suite(Winn *et al.*, 2011). The model was

497 subjected to multiple rounds of refinement in Refmac(Murshudov, Vagin and Dodson, 1997)

498 and Phenix(Adams *et al.*, 2010). The overall geometry in the final structure of the C5-K8

499 complex is good, with 97.2 % of residues in favoured regions of the Ramachandran plot and

500 no outliers.

501 The C5-K92 complex crystallised in space group C2 with 1 molecule in the asymmetric unit.

502 C5 was solved by molecular replacement with Phaser(McCoy *et al.*, 2007) using the C5-

503 OmCI-RaCI structure (PDB accession code: 5HCC), with OmCI and RaCI removed. Manual

504 building of the K92 peptide in Coot was greatly informed by mass spectroscopy disulphide

505 mapping experiments. The model was subjected to multiple rounds of manual rebuilding in

506 Coot and refinement in Phenix(Adams *et al.*, 2010). The overall geometry in the final

507 structure of the C5-K92 complex is good, with 95.2 % of residues in favoured regions of the

508 Ramachandran plot and no outliers. Structure factors and coordinates have been deposited in

509 the PDB (PDB accession codes 7AD6 and 7AD7). Crystal trials were also performed with the

510 C5-K57 and C5-K149 complexes, but the resulting crystals diffracted poorly.

511 **Disulphide mapping of K92 peptide.** 250 µL K92 peptide at 1 mg/mL was reduced with 6

512 µL of 0.5 M Dithiothreitol (Thermo Fisher) for 40 minutes at 37 °C and alkylated with

513   addition of 18 µL of 2-Iodoacetamide (Thermo Fisher), at room temperature for 30 minutes.

514   Overnight dialysis into assay buffer (7.5mM Tris-HCl, 1.5mM CaCl$_2$, pH 7.9) was performed

515   using 2 kDa slide-a-lyzer cassettes (Thermo Fisher). Chymotrypsin (sequencing grade, Roche

516   Applied Sciences) was reconstituted to 1 µg/µL in assay buffer and 5 µL of reconstituted

517   enzyme was added to 80 µL of sample. Once mixed, the sample was incubated at 37 °C for

518   1.5 hours before being quenched with 5 µL of 1 % TFA. Samples were diluted 1 in 10 and 5

519   µL was loaded onto the analytical column.

520   Liquid Chromatography electrospray ionisation mass spectrometry was acquired using an

521   Ultimate 3000 UHPLC system (Thermo Fisher Scientific, San Jose, CA) coupled with a Q-

522   Exactive Plus Orbitrap (Thermo Fisher Scientific). Separations were performed using

523   gradient elution (A: 0.1 % Formic acid, B: 0.1 % Formic acid in acetonitrile) on an Acquity

524   UPLC BEH C18 Column (130 Å, 1.7 µm, 2.1 mm X 150 mm; Waters Corp., Milford, MA,

525   USA) with the column temperature maintained at 40 °C.

526   The following analytical gradient at 0.2 mL/min was used: 1 % B was held for 2 minutes, 1-

527   36 % B over 28 minutes, 36-50 % over 5 minutes, 50-99 % B over 0.5 minutes. There were

528   sequential wash steps with changes in gradient of 99 %-1 % B over 0.5 minutes (at a higher

529   flow rate of 0.5 mL/min) before equilibration at 1 % B for 6.5 minutes (at the original 0.2

530   mL/min).

531   A Full MS / dd-MS2 (Top 5) scan was run in positive mode. Full MS: scan range was 200 to

532   2000 m/z with 70,000 resolution (at 200 m/z) and a 3 x 10^6 AGC target, 100 ms maximum

533   Injection time. The dd-MS2: 2.0 m/z isolation window, CID fragmentation (NCE 28) with

534   fixed first mass of 140.0 m/z, with a 17,500 resolution (at 200 m/z), 1 x 10^5 AGC target, 200

535   ms maximum injection time. The source conditions of the MS were capillary voltage; 3 kV,

536   S-lens RF level; 50, Sheath gas flow rate; 25, Auxiliary gas flow rate; 10, Auxiliary gas

537   heater temp; 150 °C and the MS inlet capillary was maintained at 320 °C.

538   Data were acquired using Xcalibur™ 4.0 software (Thermo Fisher Scientific), and raw files

539   were analysed by peptide mapping analysis using Biopharma Finder 2.0 software (Thermo

540   Fisher Scientific) by performing a disulphide bond search with a chymotrypsin (medium

541   specificity) digest against the K92 peptide sequence. Assignments and integrations from

542   Biopharma Finder were filtered to include only peptides identified as containing a single

543   disulphide bond and with an experimental mass within |5| ppm of the theoretical mass.

18

544   Intensities for all peptides containing the same cysteines pairing were summed and

545   percentages were obtained from the summed against total intensities.

546   **Binding pose metadynamics**. Simulation structures were prepared using Schrodinger's

547   Maestro Protein preparation wizard. The molecular dynamics runs were performed using the

548   Schrodinger's default implementation of the binding pose metadynamics with the peptide

549   chain considered in place of a ligand. Additional RMSD calculations for the peptide internal

550   structure assessment in the last 20% of the dynamics were performed relative to the starting

551   structures.

552   **Small angle X-ray scattering (SAXS)** Data was collected at the EMBL P12 beam line

553   (PETRA III, DESY Hamburg, Germany(Blanchet *et al.*, 2015)). Data was collected with

554   inline size exclusion chromatography (SEC) mode, using the Agilent 1260 Infinity II Bio-

555   inert LC. 50 μL of complement component C5 at 31.6 μM (5.96 mg/ml) was injected onto a

556   Superdex 200 Increase 5/150 column (GE Healthcare) at a flow rate of 0.35 ml/min. The

557   mobile phase was comprised of 20mM Tris pH 7.35, 75mM NaCl, and 3% glycerol. The

558   column elute was directly streamed to the SAXS capillary cell, and throughout the 15-

559   minute-run 900 frames of 1 sec exposure were collected. After data reduction and radial

560   averaging the program CHROMIXS(Panjkovich and Svergun, 2018) was employed. Around

561   100 statistically similar buffer frames were selected and used for background subtraction of

562   the sample frames from the chromatographic peak. This results in the final I(s) vs s scattering

563   profiles, where s = $4\pi\sin\theta/\lambda$, 2θ is the scattering angle and λ = 1.24 Å. The scattering data in

564   the momentum transfer range $0.05 < s < 0.32$ nm^{-1} were collected with a PILATUS 6M pixel

565   detector at a distance of 3.1 m from the sample.

566   ATSAS 2.8(Franke *et al.*, 2017) was employed for further data analysis and modelling. The

567   program PRIMUS(Konarev *et al.*, 2003) was used to perform Guinier analysis (lnI(s) versus

568   s^2) from which the radius of gyration, R_G, was determined. Distance probability functions,

569   p(r), were calculated using the inverse Fourier transformation method implemented in

570   GNOM(Svergun, 1992) that provided the maximum particle dimension, D_{max}. The

571   concentration-independent molecular weight estimate, MW_{VC},is based on the volume of

572   correlation(Rambo and Tainer, 2013). The values are reported in Supplementary 3.1.

573   Theoretical scattering profiles were computed from X-ray coordinates using Crysol(Svergun,

574   Barberato and Koch, 1995) and SREFLEX(Panjkovich and Svergun, 2016) was used to refine

575   the models. For this, the program partitions the structure into pseudo-domains and

19

576   hierarchically employs NMA to find the domain rearrangements minimizing the discrepancy

577   χ^2 between the SAXS curve computed from the refined model and the experimental data.

578   On the same day, multi-angle laser light scattering (MALLS) data were collected with a

579   separate SEC run under the same experimental conditions (set-up, buffer, run parameters

580   etc.). For this, a Wyatt Technologies miniDAWN TREOS multiangle laser light scattering

581   detector coupled to an OptiLab T-Rex differential refractometer for protein concentration

582   determination (dn/dc was taken as 0.185) was used. The MALLS system was calibrated

583   relative to the scattering from toluene. The MWMALLS distribution of species eluting from

584   the SEC column were determined with the Wyatt ASTRA7 software package.

585   The experimental SAXS data and the models derived from them were deposited to the Small

586   Angle Scattering Biological Data Bank (accession number: SASDJA6).

587   **Hydrogen/deuterium mass spectrometry** 6 µM of C5 was incubated with 10 µM of peptide

588   (K8, K92 or K57) to achieve complex during deuterium exchange conditions. 4 µL of C5 or

589   the C5-peptide complex were diluted into 57 µL of 10 mM phosphate in H_2O (pH 7.0), or

590   into 10 mM phosphate in D_2O (pD 7.0) at 25 °C. The deuterated samples were then incubated

591   for 0.5, 2, 15 and 60 minutes at 25 °C. After the reaction, all samples were quenched by

592   mixing at 1:1 (*v/v*) with a quench buffer (4 M Guanadine Hydrochloride, 250 mM Tris (2-

593   carboxyethyl) phosphine hydrochloride (TCEP), 100 mM phosphate) at 1 °C. The final

594   mixed solution was pH 2.5. The mixture was the immediately injected into the nanoAcquity

595   HDX module (Waters Corp.) for peptic digest, using an enzymatic online digestion column

596   (Waters Corp.) in 0.2 % formic acid in water at 20 °C and with a flow rate of 100 µL/min. All

597   deuterated time points and un-deuterated controls were carried out in triplicate with blanks

598   run between each data-point.

599   Peptide fragments were then trapped using an Acquity BEH C18 1.7 µM VANGUARD

600   chilled pre-column for 3 min. Peptides were eluted into a chilled Acquity UPLC BEH C18

601   1.7 µm 1.0×100 using the following gradient: 0 minute, 5 % B; 6 minutes, 35% B; 7

602   minutes, 40 % B; 8 minutes, 95 % B, 11 minutes, 5 % B; 12 minutes, 95 % B; 13 minutes, 5

603   % B; 14 minutes, 9 5% B; 15 minutes, 5 % B (A: 0.2 % HCOOH in H_2O, B: 0.2 % HCOOH

604   in acetonitrile. The trap and UPLC columns were both maintained at 0°C. Peptide fragments

605   were ionized by positive electrospray into a Synapt G2-Si mass spectrometer (Waters). Data

606   acquisition was run in ToF-only mode over an m/z range of 50-2000 Th, using an MSE

607   method (low collision energy, 4V; high collision energy: ramp from 18V to 40V). Glu-1-

20

608   Fibrinopeptide B peptide was used for internal lock mass correction. To avoid significant

609   peptide carry-over between runs, the on-line Enzymate pepsin column (Waters) was washed

610   three times with pepsin wash (0.8 % formic acid, 1.5 M Gu-HCl, 4 % MeOH) and a blank run

611   was performed between each sample run.

612   MSE data from undeuterated samples of C5 were used for sequence identification using the

613   Waters Protein Lynx Global Server 2.5.1 (PLGS). Ion accounting files for the 3 control

614   samples were combined into a peptide list imported into Dynamx v3.0 software (Waters).

615   The output peptides were subjected to further filtering in DynamX. Filtering parameters used

616   were: minimum and maximum peptide sequence length of 4 and 25, respectively, minimum

617   intensity of 1000, minimum MS/MS products of 2, minimum products per amino acid of 0.2,

618   and a maximum MH + error threshold of 10 ppm. DynamX was used to quantify the isotopic

619   envelopes resulting from deuterium uptake for each peptide at each time-point. Furthermore,

620   all the spectra were examined and checked visually to ensure correct assignment of m/z peaks

621   and only peptides with a high signal to noise ratios were used for HDX-MS analysis.

622   Following manual filtration in Dynamx, confidence intervals for differential HDX-MS

623   (ΔHDX) measurements of individual time point were calculated using Deuteros(Lau *et al.*,

624   2019) software. Only peptides which satisfied a ΔHDX confidence interval of 98 % were

625   considered significant. The ΔHDX was then plotted onto the C5 structure in Pymol.

626   **Surface plasmon resonance, single cycle kinetics.** On a Biacore 8K (GE Healthcare),

627   human C5b was immobilised on a CM5 chip (GE Healthcare). Flow cells were activated

628   using a standard immobilisation protocol: EDC/NHS was mixed at 1:1 ratio (flow rate, 10

629   µL/min; contact time, 30 seconds). C5b, at 1 µg/mL in pH 4.5 sodium-acetate buffer, was

630   immobilized on flow cell two only (flow rate, 10 µL/min; contact time, 420 seconds). Finally,

631   ethanolamine was applied to both flow cells (flow rate, 10 µL/min; contact time, 420

632   seconds). A final immobilization level of 500-700 response units was obtained.

633   Single-cycle kinetics were measured using a 7-point, 3-fold serial dilution (spanning a range

634   of 1 µM to 1.4 nM) in HBS-EP buffer (GE healthcare). A high flow rate of 40 µL/min was

635   used, with a contact time of 300 seconds and a dissociation time of 2700 seconds. Binding to

636   the reference surface was subtracted, and the data were fitted to a single-site binding model

637   using Biacore evaluation software. All sensorgrams were inspected for evidence of mass

638   transport limitation using the flow rate-independent component of the mass transfer constant

639   (tc).

21

640 **Surface plasmon resonance, cross-blocking.** On a Biacore 8K (GE Healthcare), human C5,

641 was amine coupled to a CM5 chip, using the same protocol as for C5b. A final

642 immobilization level of approximately 1000-2000 response units was obtained. For cross

643 blocking, the surface was saturated with two sequential injections of a 20 µM knob domain

644 solution in HBS-EP buffer (GE healthcare), using a flow rate of 30 µL/min and contact time

645 of 300 seconds. This was immediately followed with an injection of a second knob domain

646 peptide, again at 20 µM in HBS-EP, with a flow rate of 30 µL/min and a contact time of 270

647 seconds, the dissociation phase was measured for 600 seconds. Binding to the reference

648 surface was subtracted, and sensorgrams were plotted in Graphpad Prism software.

Competing Interests

650 This work was performed by A.M. as partial fulfilment of the requirements for a PhD from

651 the University of Bath and was funded by UCB. A.M., S.S., V.O., J.S., B.H., V.E., Z.A. and

652 A.D.G.L are present or past employees of UCB and may hold shares and/or stock options.

653 T.E.M is a Board member of Ra Pharmaceuticals, Inc. All other authors declare no competing

654 interests.

Acknowledgements

656 We would like to thank John Cashman for his help during crystallography screening.

Author Contribution

658 A.M., A.D.G.L. and J.v.d.E. designed the study. The manuscript was written by A.M.,

659 A.D.G.L. and J.v.d.E., with input from all authors. A.M expressed and purified peptides.

660 P.H.N. and T.E.M. purified complement proteins. In vitro assays were performed by A.M and

661 M.L. Crystallography was performed by A.M with assistance from J.R.B, S.S, S.C and

662 J.v.d.E. Disulphide mapping was performed by B.H. Comparative antibody analysis was

663 performed by S.R., J.S. and C.M.D. Binding pose metadynamics was by V.O. SAXS

664 experiments were performed by M.G. and D.S. and HDX-MS by Z.A. and V.E. SPR was

665 performed by A.M. Supervision was by A.D.G.L and J.v.d.E.
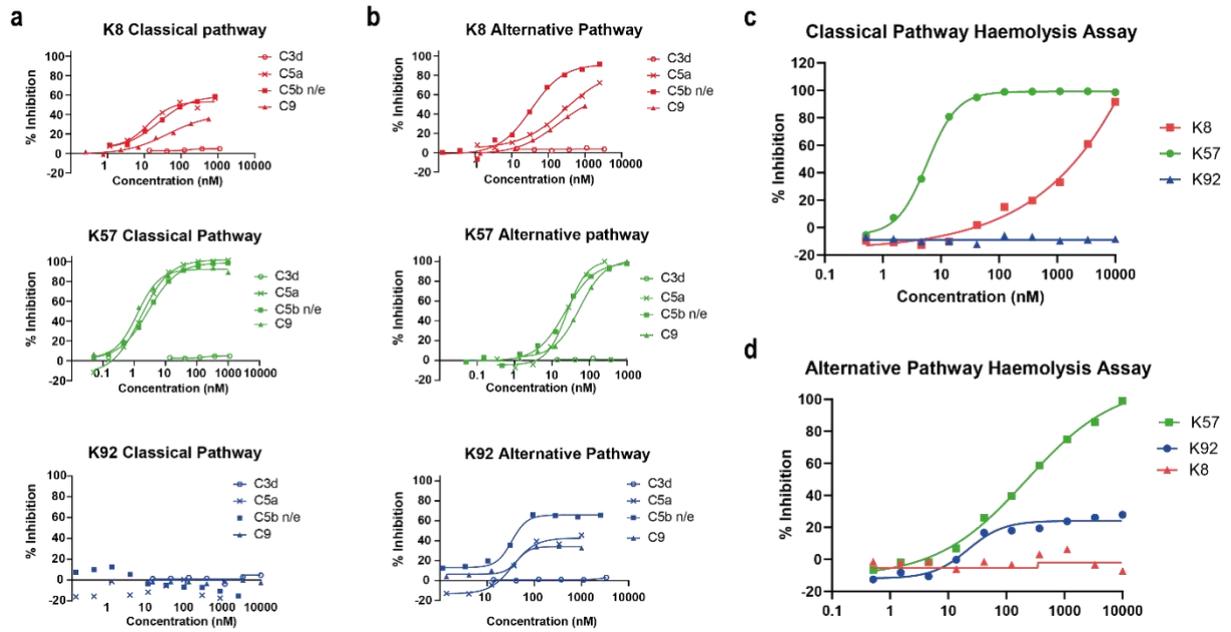
Figure 1. Functional modulation of C5 via knob domain peptides. Classical pathway (CP) driven ELISA assays (a) and alternative pathway (AP) driven ELISA assays (b) are shown. For both pathways, the inhibition of 3d deposition, C5b neo-epitope formation, C5a release and C9 deposition were tracked. Haemolysis assays with sheep erythrocytes, for the CP (c), and rabbit erythrocytes, for the AP (d), show that K57 is a potent and efficacious inhibitor of both pathways. K92 is selective, partial antagonist of the AP, while K8 is a weak antagonist of the CP but did not show efficacy in the AP haemolysis assay, below 10 µM.
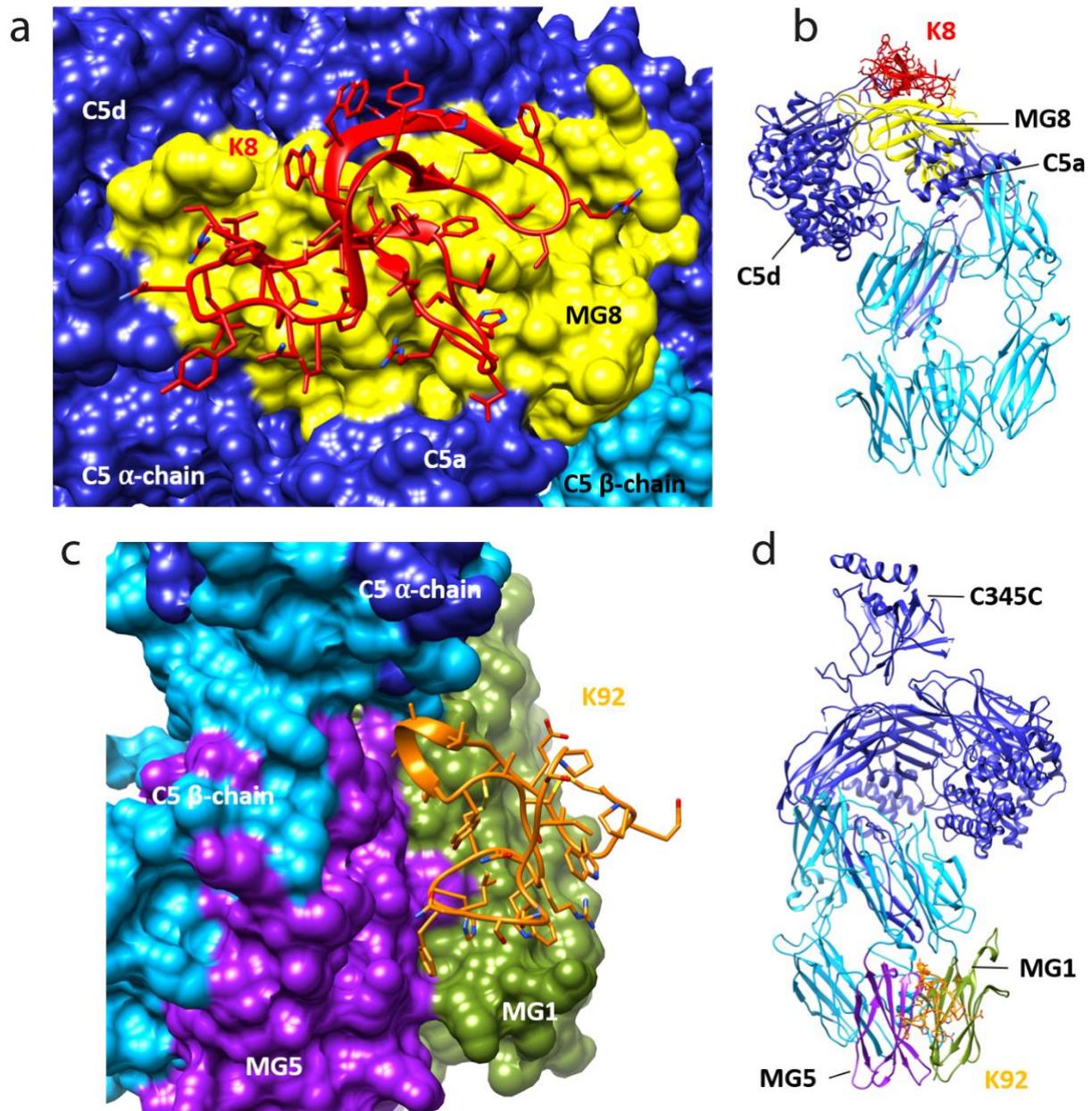
Figure 2. Knob domain crystal structures. Panels a and b show the crystal structure of C5 in complex with the K8 knob domain peptide. The K8 epitope is located on a previously unreported ligand binding site on the MG8 domain of C5 (a). The entire structure is shown (b), notably, electron density for the flexible C345C domain of C5 was absent, preventing building of this domain in the structure. The crystal structure of C5 in complex with the K92 knob domain peptide is shown (panels c and d). The K92 epitope is located between the MG1 and MG5 domains.
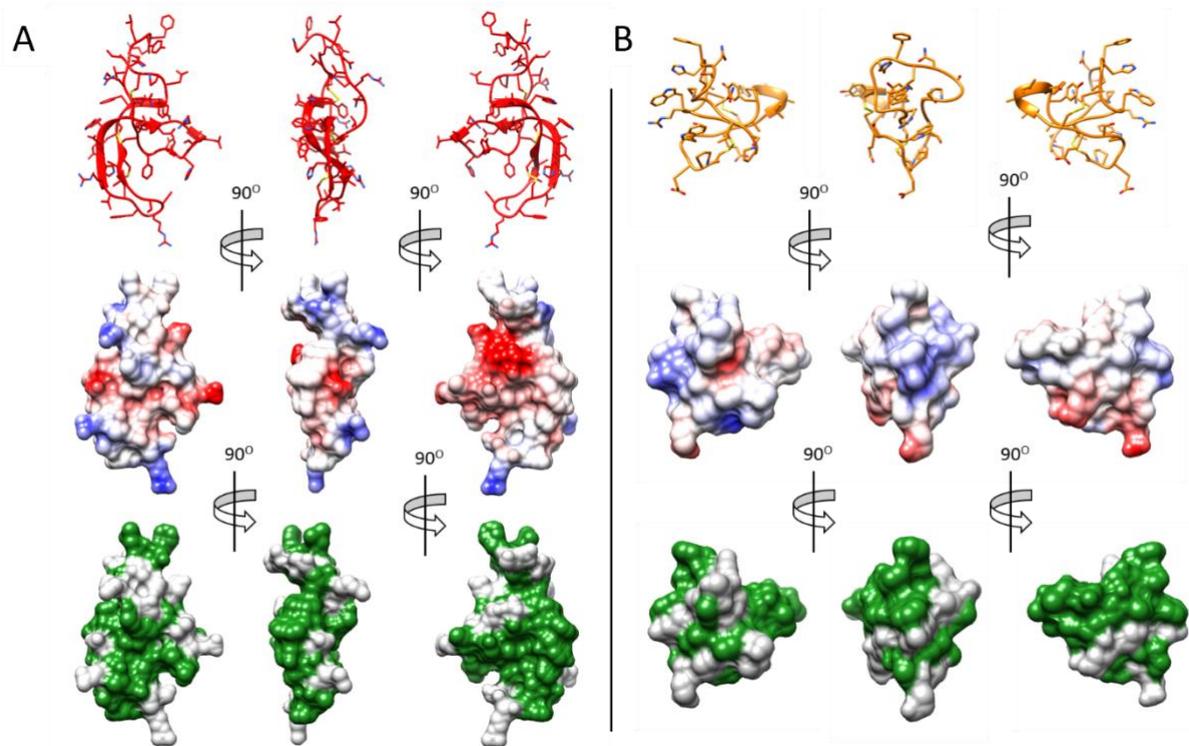
Figure 3. The hydrophobic paratopes of knob domains. The K8 and K92 knob domain peptides are shown in panels a and b, respectively. For each, the binding face is shown in the first column, with a 90° rotation shown in the second column and a further 90° rotation in the third columns shows the opposing, non-binding face of each domain. In the top row the amino acid side chains and disulphide bonds are shown in addition to the secondary structure. Using UCSF Chimera(Pettersen *et al.*, 2004), surface visualisation and coulombic colouring has been applied to denote charge in the middle row, with blue denoting positively charged residues and red negatively charged. The bottom row shows colouring of the non-polar residues, highlighting the hydrophobic nature of the knob domain paratopes.
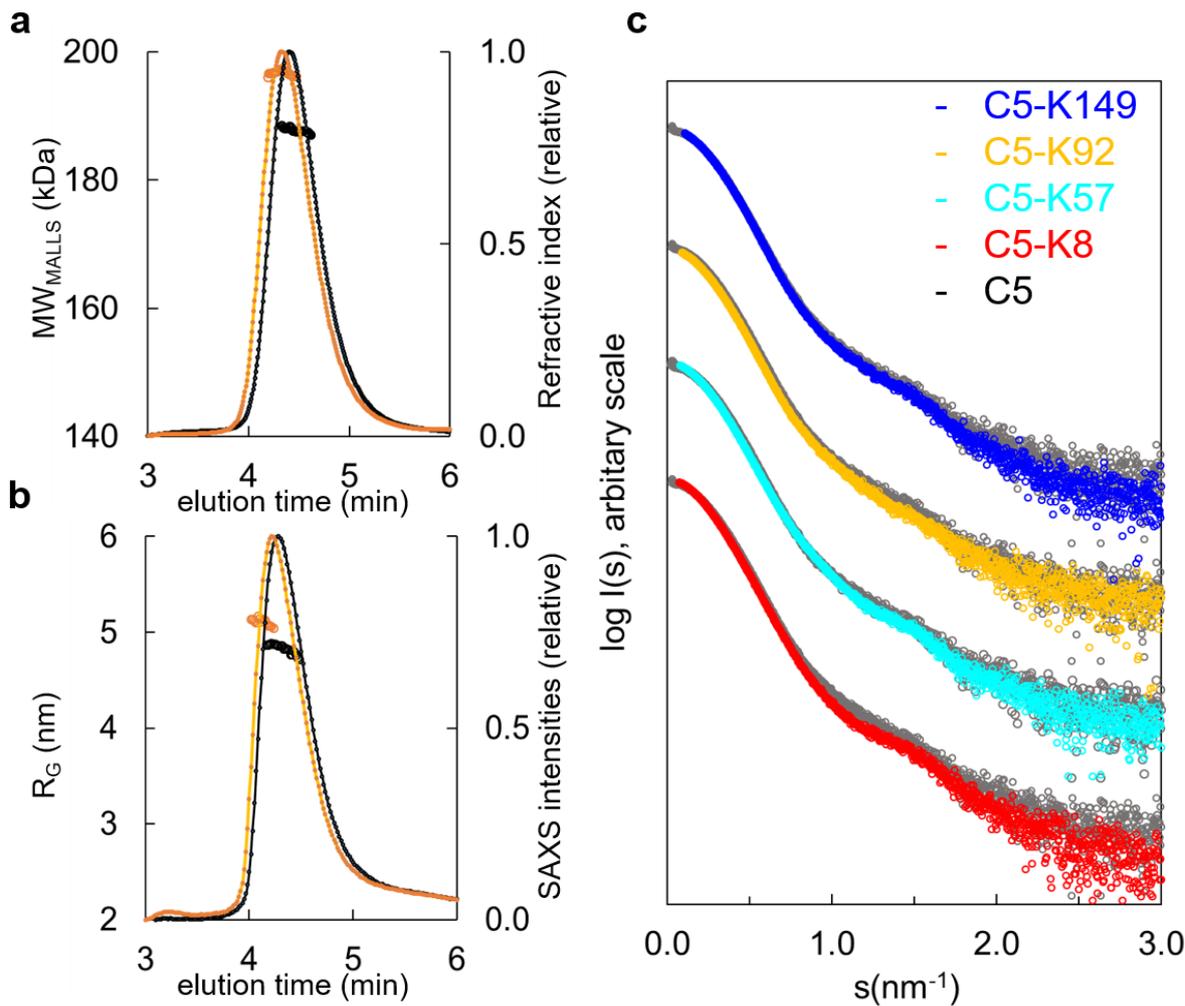
Figure 4. Hydrodynamic properties and solution conformation of C5 and C5-knob domain complexes by SAXS.

SEC-MALLS chromatograms (a) for apo C5 (black) and C5-K92 (orange), show a homogenous molecular weight increase across the C5-K92 elution peak. The SEC-SAXS elution profile collected under identical experimental conditions (b) shows an increase in radius of gyration (R_G) for the C5-K92 complex. Scattering curves of all C5-knob domains are shown (c), the C5-knob domain complexes are shown against apo C5 (in grey), for ease of viewing the curves are arbitrarily shifted in the Y axis.
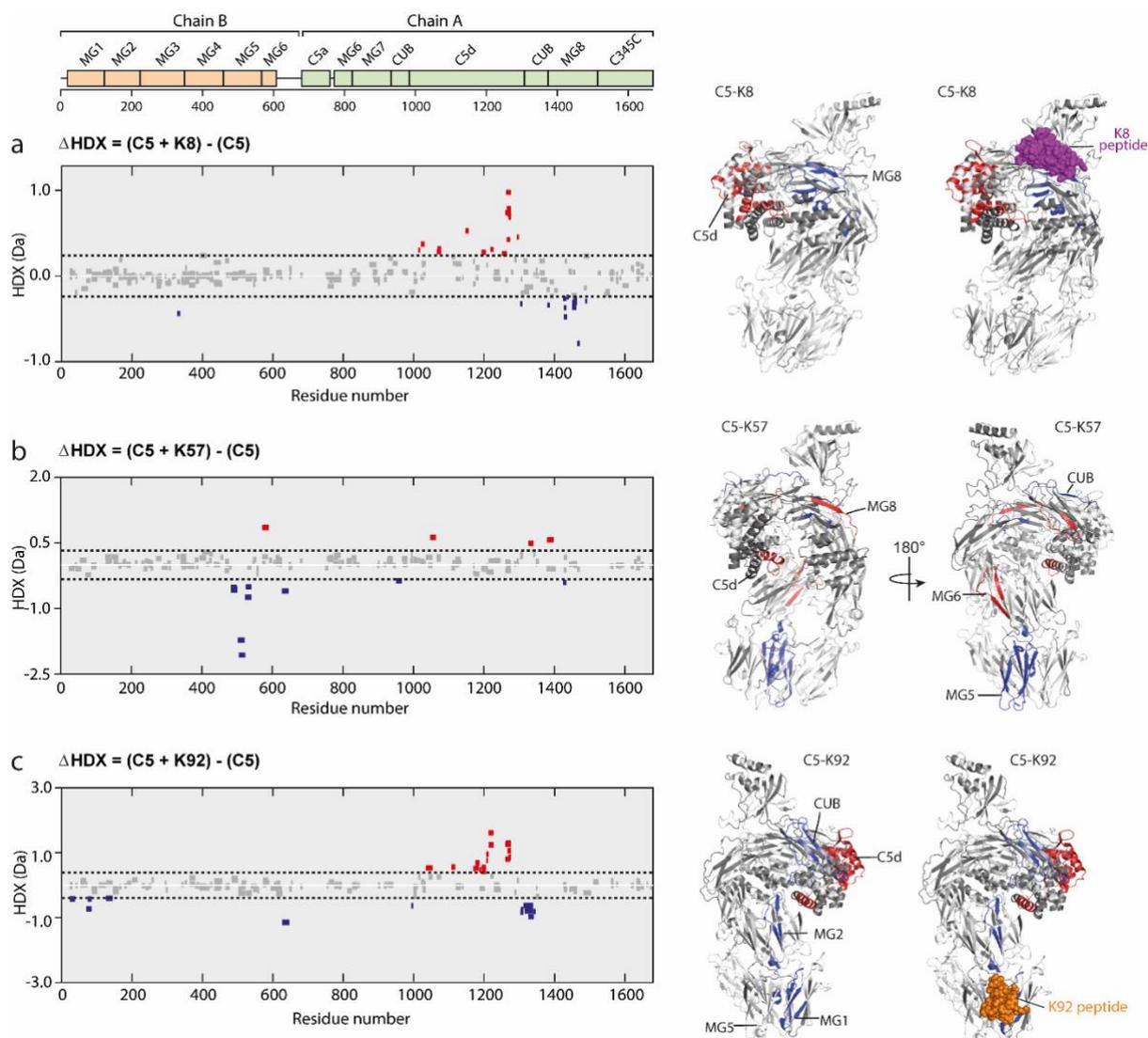
Figure 5. Impact of knob domain binding on the structural dynamics and conformation of C5. Differential HDX (ΔHDX) plots for C5 in complex with knob domains (a) K8, (b) K57 and (c) K92 at 1 hour of deterium exposure. Blue denotes peptides with decreased HDX (backbone H-bond stabilisation) and red denotes peptides with increased HDX (backbone H-bond destabilisation). 98% confidence intervals are shown as dotted lines. Peptides in grey have insignificant ΔHDX. Measurements were performed at in triplicate and all HDX-MS peptide data is detailed in Supporting Table XX. ΔHDX for C5 +K8, C5 + K57 and C5 + K92 are coloured onto C5 (PDB accession: 5HCC, minus OmCI and RaCI).
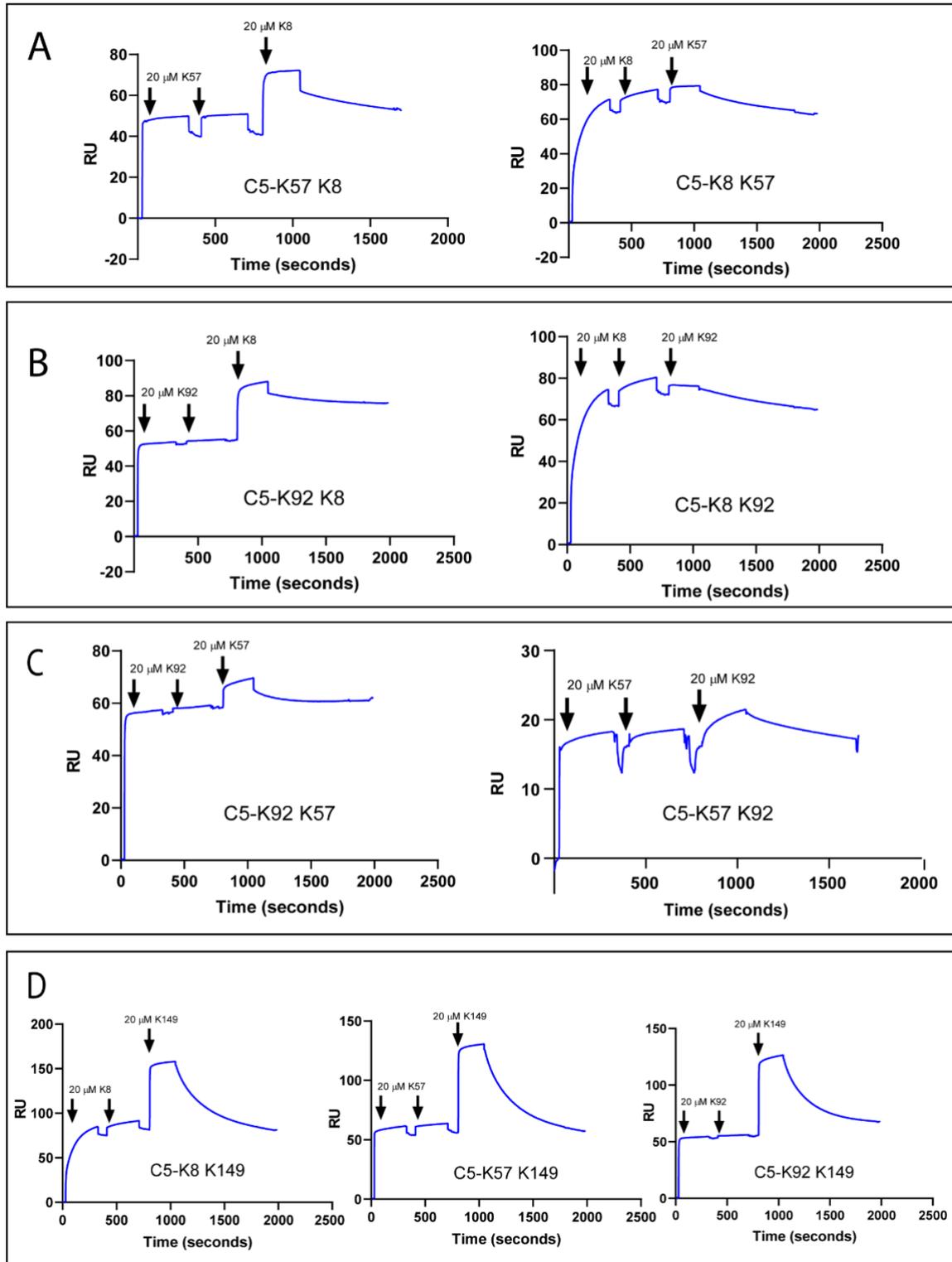
Figure 6. Surface plasmon resonance: cross blocking. Panels A, B and C highlight negative cooperativity between the K8, K92 and K57 peptides. Neither K57 or K92 can bind to the C5-K8 complex but K8 can bind, albeit at a lower level to, C5-K57 and C5-K92. We could not detect any negative cooperativity between K8, K57 or K92 with the silent binder K149, shown in panel D.

References

Adams, P. D., Afonine, P. V., Bunkoczi, G., Chen, V. B., Davis, I. W., Echols, N., Headd, J. J., Hung, L. W., Kapral, G. J., Grosse-Kunstleve, R. W., McCoy, A. J., Moriarty, N. W., Oeffner, R., Read, R. J., Richardson, D. C., Richardson, J. S., Terwilliger, T. C. and Zwart, P. H. (2010) 'PHENIX: a comprehensive Python-based system for macromolecular structure solution', *Acta Crystallogr D Biol Crystallogr,* 66(Pt 2), pp. 213-21.

Aleshin, A. E., DiScipio, R. G., Stec, B. and Liddington, R. C. (2012) 'Crystal structure of C5b-6 suggests structural basis for priming assembly of the membrane attack complex', *J Biol Chem,* 287(23), pp. 19642-52.

Bestebroer, J., Aerts, P. C., Rooijakkers, S. H., Pandey, M. K., Kohl, J., van Strijp, J. A. and de Haas, C. J. (2010) 'Functional basis for complement evasion by staphylococcal superantigen-like 7', *Cell Microbiol,* 12(10), pp. 1506-16.

Biesecker, G., Dihel, L., Enney, K. and Bendele, R. A. (1999) 'Derivation of RNA aptamer inhibitors of human complement C5', *Immunopharmacology,* 42(1-3), pp. 219-30.

Blanchet, C. E., Spilotros, A., Schwemmer, F., Graewert, M. A., Kikhney, A., Jeffries, C. M., Franke, D., Mark, D., Zengerle, R., Cipriani, F., Fiedler, S., Roessle, M. and Svergun, D. I. (2015) 'Versatile sample environments and automation for biological solution X-ray scattering experiments at the P12 beamline (PETRA III, DESY)', *J Appl Crystallogr,* 48(Pt 2), pp. 431-443.

Borodovsky, A., Yucius, K., Sprague, A., Banda, N. K., Holers, V. M., Vaishnaw, A., Maier, M., Kallanthottathil, R., Charisse, K., Kuchimanchi, S., Manoharan, M., Salant, D. J., Fitzgerald, K., Meyers, R. and Sorensen, B. (2014) 'Aln-CC5, an Investigational RNAi Therapeutic Targeting C5 for Complement Inhibition', *Blood,* 124(21), pp. 1606-1606.

Clark, A. J., Tiwary, P., Borrelli, K., Feng, S., Miller, E. B., Abel, R., Friesner, R. A. and Berne, B. J. (2016) 'Prediction of Protein-Ligand Binding Poses via a Combination of Induced Fit Docking and Metadynamics Simulations', *J Chem Theory Comput,* 12(6), pp. 2990-8.

DiScipio, R. G. (1992) 'Formation and structure of the C5b-7 complex of the lytic pathway of complement', *J Biol Chem,* 267(24), pp. 17087-94.

Dunbar, J., Krawczyk, K., Leem, J., Baker, T., Fuchs, A., Georges, G., Shi, J. and Deane, C. M. (2014) 'SAbDab: the structural antibody database', *Nucleic Acids Res,* 42(Database issue), pp. D1140-6.

Emsley, P., Lohkamp, B., Scott, W. G. and Cowtan, K. (2010) 'Features and development of Coot', *Acta Crystallogr D Biol Crystallogr,* 66(Pt 4), pp. 486-501.

Franke, D., Petoukhov, M. V., Konarev, P. V., Panjkovich, A., Tuukkanen, A., Mertens, H. D. T., Kikhney, A. G., Hajizadeh, N. R., Franklin, J. M., Jeffries, C. M. and Svergun, D. I. (2017) 'ATSAS 2.8: a comprehensive data analysis suite for small-angle scattering from macromolecular solutions', *J Appl Crystallogr,* 50(Pt 4), pp. 1212-1225.

Fredslund, F., Laursen, N. S., Roversi, P., Jenner, L., Oliveira, C. L., Pedersen, J. S., Nunn, M. A., Lea, S. M., Discipio, R., Sottrup-Jensen, L. and Andersen, G. R. (2008) 'Structure of and influence of a tick complement inhibitor on human complement component 5', *Nat Immunol,* 9(7), pp. 753-60.

Fusani, L., Palmer, D. S., Somers, D. O. and Wall, I. D. (2020) 'Exploring Ligand Stability in Protein Crystal Structures Using Binding Pose Metadynamics', *J Chem Inf Model,* 60(3), pp. 1528-1539.

Gorrec, F. (2009) 'The MORPHEUS protein crystallization screen', *J Appl Crystallogr,* 42(Pt 6), pp. 1035-1042.

Hadders, M. A., Bubeck, D., Roversi, P., Hakobyan, S., Forneris, F., Morgan, B. P., Pangburn, M. K., Llorca, O., Lea, S. M. and Gros, P. (2012) 'Assembly and regulation of the membrane attack complex based on structures of C5b6 and sC5b9', *Cell Rep,* 1(3), pp. 200-7.

Haselbach, D., Schrader, J., Lambrecht, F., Henneberg, F., Chari, A. and Stark, H. (2017) 'Long-range allosteric regulation of the human 26S proteasome by 20S proteasome-targeting cancer drugs', *Nat Commun,* 8, pp. 15578.

Holm, L. (2020) 'DALI and the persistence of protein shape', *Protein Sci,* 29(1), pp. 128-140.

Hutchinson, J. M., Mesa, K. A., Alexander, D. L., Yu, B., O'Rourke, S. M., Limoli, K. L., Wrin, T., Deeks, S. G. and Berman, P. W. (2019) 'Unusual Cysteine Content in V1 Region of gp120 From an Elite Suppressor That Produces Broadly Neutralizing Antibodies', *Front Immunol*, 10, pp. 1021.

Jendza, K., Kato, M., Salcius, M., Srinivas, H., De Erkenez, A., Nguyen, A., McLaughlin, D., Be, C., Wiesmann, C., Murphy, J., Bolduc, P., Mogi, M., Duca, J., Namil, A., Capparelli, M., Darsigny, V., Meredith, E., Tichkule, R., Ferrara, L., Heyder, J., Liu, F., Horton, P. A., Romanowski, M. J., Schirle, M., Mainolfi, N., Anderson, K. and Michaud, G. A. (2019) 'A small-molecule inhibitor of C5 complement protein', *Nature Chemical Biology*, 15(7), pp. 666-668.

Jore, M. M., Johnson, S., Sheppard, D., Barber, N. M., Li, Y. I., Nunn, M. A., Elmlund, H. and Lea, S. M. (2016) 'Structural basis for therapeutic inhibition of complement C5', *Nat Struct Mol Biol*, 23(5), pp. 378-86.

Jubb, H. (2015) 'Arpeggio: An interatomic interaction calculation web server available at http://structure.bioc.cam.ac.uk/arpeggio.'.

Klein, M. T., Vinson, P. N. and Niswender, C. M. (2013) 'Approaches for probing allosteric interactions at 7 transmembrane spanning receptors', *Prog Mol Biol Transl Sci*, 115, pp. 1-59.

Konarev, P. V., Volkov, V. V., Sokolova, A. V., Koch, M. H. J. and Svergun, D. I. (2003) 'PRIMUS: a Windows PC-based system for small-angle scattering data analysis', *Journal of Applied Crystallography*, 36(5), pp. 1277-1282.

Krissinel, E. and Henrick, K. (2007) 'Inference of macromolecular assemblies from crystalline state', *J Mol Biol*, 372(3), pp. 774-97.

Langer, G., Cohen, S. X., Lamzin, V. S. and Perrakis, A. (2008) 'Automated macromolecular model building for X-ray crystallography using ARP/wARP version 7', *Nat Protoc*, 3(7), pp. 1171-9.

Lau, A. M. C., Ahdash, Z., Martens, C. and Politis, A. (2019) 'Deuteros: software for rapid analysis and visualization of data from differential hydrogen deuterium exchange-mass spectrometry', *Bioinformatics*, 35(17), pp. 3171-3173.

Lau, J. L. and Dunn, M. K. (2018) 'Therapeutic peptides: Historical perspectives, current development trends, and future directions', *Bioorg Med Chem*, 26(10), pp. 2700-2707.

Laursen, N. S., Andersen, K. R., Braren, I., Spillner, E., Sottrup-Jensen, L. and Andersen, G. R. (2011) 'Substrate recognition by complement convertases revealed in the C5-cobra venom factor complex', *EMBO J*, 30(3), pp. 606-16.

Laursen, N. S., Gordon, N., Hermans, S., Lorenz, N., Jackson, N., Wines, B., Spillner, E., Christensen, J. B., Jensen, M., Fredslund, F., Bjerre, M., Sottrup-Jensen, L., Fraser, J. D. and Andersen, G. R. (2010) 'Structural basis for inhibition of complement C5 by the SSL7 protein from Staphylococcus aureus', *Proc Natl Acad Sci U S A*, 107(8), pp. 3681-6.

Lee, A. C., Harris, J. L., Khanna, K. K. and Hong, J. H. (2019) 'A Comprehensive Review on Current Advances in Peptide Drug Development and Design', *Int J Mol Sci*, 20(10).

Long, F., Vagin, A. A., Young, P. and Murshudov, G. N. (2008) 'BALBES: a molecular-replacement pipeline', *Acta Crystallogr D Biol Crystallogr*, 64(Pt 1), pp. 125-32.

Macpherson, A., Liu, X., Dedi, N., Kennedy, J., Carrington, B., Durrant, O., Heywood, S., van den Elsen, J. and Lawson, A. D. G. (2018) 'The rational design of affinity-attenuated OmCI for the purification of complement C5', *J Biol Chem*, 293(36), pp. 14112-14121.

Macpherson, A., Scott-Tucker, A., Spiliotopoulos, A., Simpson, C., Staniforth, J., Hold, A., Snowden, J., Manning, L., van den Elsen, J. and Lawson, A. D. G. (2020) 'Isolation of antigen-specific, disulphide-rich knob domain peptides from bovine antibodies', *PLoS Biol*, 18(9), pp. e3000821.

McCoy, A. J., Grosse-Kunstleve, R. W., Adams, P. D., Winn, M. D., Storoni, L. C. and Read, R. J. (2007) 'Phaser crystallographic software', *J Appl Crystallogr*, 40(Pt 4), pp. 658-674.

McNamara, L. A., Topaz, N., Wang, X., Hariri, S., Fox, L. and MacNeil, J. R. (2017) 'High Risk for Invasive Meningococcal Disease Among Patients Receiving Eculizumab (Soliris) Despite Receipt of Meningococcal Vaccine', *MMWR Morb Mortal Wkly Rep*, 66(27), pp. 734-737.

Murshudov, G. N., Vagin, A. A. and Dodson, E. J. (1997) 'Refinement of macromolecular structures by the maximum-likelihood method', *Acta Crystallogr D Biol Crystallogr*, 53(Pt 3), pp. 240-55.

Nurnberger, J., Philipp, T., Witzke, O., Opazo Saez, A., Vester, U., Baba, H. A., Kribben, A., Zimmerhackl, L. B., Janecke, A. R., Nagel, M. and Kirschfink, M. (2009) 'Eculizumab for atypical hemolytic-uremic syndrome', *N Engl J Med,* 360(5), pp. 542-4.

Panjkovich, A. and Svergun, D. I. (2016) 'Deciphering conformational transitions of proteins by small angle X-ray scattering and normal mode analysis', *Phys Chem Chem Phys,* 18(8), pp. 5707-19.

Panjkovich, A. and Svergun, D. I. (2018) 'CHROMIXS: automatic and interactive analysis of chromatography-coupled small-angle X-ray scattering data', *Bioinformatics,* 34(11), pp. 1944-1946.

Pettersen, E. F., Goddard, T. D., Huang, C. C., Couch, G. S., Greenblatt, D. M., Meng, E. C. and Ferrin, T. E. (2004) 'UCSF Chimera--a visualization system for exploratory research and analysis', *J Comput Chem,* 25(13), pp. 1605-12.

Rambo, R. P. and Tainer, J. A. (2013) 'Accurate assessment of mass, models and resolution by small-angle scattering', *Nature,* 496(7446), pp. 477-81.

Reichhardt, M. P., Johnson, S., Tang, T., Morgan, T., Tebeka, N., Popitsch, N., Deme, J. C., Jore, M. M. and Lea, S. M. (2020) 'An inhibitor of complement C5 provides structural insights into activation', *Proc Natl Acad Sci U S A,* 117(1), pp. 362-370.

Ricardo, A., Arata, M., DeMarco, S. J., Dhamnaskar, K., Hammer, R., Josephson, K., Seyb, K., Tobe, S., Wang, Z., Zheng, H. and Treco, D. (2014) 'Development of RA101348, a Potent Cyclic Peptide Inhibitor of C5 for Complement-Mediated Diseases', *Blood,* 124(21), pp. 2936-2936.

Romay-Penabad, Z., Carrera Marin, A. L., Willis, R., Weston-Davies, W., Machin, S., Cohen, H., Brasier, A. and Gonzalez, E. B. (2014) 'Complement C5-inhibitor rEV576 (coversin) ameliorates in-vivo effects of antiphospholipid antibodies', *Lupus,* 23(12), pp. 1324-6.

Rother, R. P., Rollins, S. A., Mojcik, C. F., Brodsky, R. A. and Bell, L. (2007) 'Discovery and development of the complement inhibitor eculizumab for the treatment of paroxysmal nocturnal hemoglobinuria', *Nat Biotechnol,* 25(11), pp. 1256-64.

Schatz-Jakobsen, J. A., Zhang, Y., Johnson, K., Neill, A., Sheridan, D. and Andersen, G. R. (2016) 'Structural Basis for Eculizumab-Mediated Inhibition of the Complement Terminal Pathway', *J Immunol,* 197(1), pp. 337-44.

Smith, K., Pace, A., Ortiz, S., Kazani, S. and Rottinghaus, S. (2020) 'A Phase 3 Open-label, Randomized, Controlled Study to Evaluate the Efficacy and Safety of Intravenously Administered Ravulizumab Compared with Best Supportive Care in Patients with COVID-19 Severe Pneumonia, Acute Lung Injury, or Acute Respiratory Distress Syndrome: A structured summary of a study protocol for a randomised controlled trial', *Trials,* 21(1), pp. 639.

Sok, D., Le, K. M., Vadnais, M., Saye-Francisco, K. L., Jardine, J. G., Torres, J. L., Berndsen, Z. T., Kong, L., Stanfield, R., Ruiz, J., Ramos, A., Liang, C. H., Chen, P. L., Criscitiello, M. F., Mwangi, W., Wilson, I. A., Ward, A. B., Smider, V. V. and Burton, D. R. (2017) 'Rapid elicitation of broadly neutralizing antibodies to HIV by immunization in cows', *Nature,* 548(7665), pp. 108-111.

Stanfield, R. L., Berndsen, Z. T., Huang, R., Sok, D., Warner, G., Torres, J. L., Burton, D. R., Ward, A. B., Wilson, I. A. and Smider, V. V. (2020) 'Structural basis of broad HIV neutralization by a vaccine-induced cow antibody', *Sci Adv,* 6(22), pp. eaba0468.

Svergun, D. (1992) 'Determination of the regularization parameter in indirect-transform methods using perceptual criteria', *Journal of Applied Crystallography,* 25(4), pp. 495-503.

Svergun, D., Barberato, C. and Koch, M. H. J. (1995) 'CRYSOL - a Program to Evaluate X-ray Solution Scattering of Biological Macromolecules from Atomic Coordinates', *Journal of Applied Crystallography,* 28(6), pp. 768-773.

Wilkinson, T., Dixon, R., Page, C., Carroll, M., Griffiths, G., Ho, L. P., De Soyza, A., Felton, T., Lewis, K. E., Phekoo, K., Chalmers, J. D., Gordon, A., McGarvey, L., Doherty, J., Read, R. C., Shankar-Hari, M., Martinez-Alier, N., O'Kelly, M., Duncan, G., Walles, R., Sykes, J., Summers, C., Singh, D. and Collaborators, A. (2020) 'ACCORD: A Multicentre, Seamless, Phase 2 Adaptive Randomisation Platform Study to Assess the Efficacy and Safety of Multiple Candidate Agents for the Treatment of COVID-19 in Hospitalised Patients: A structured summary of a study protocol for a randomised controlled trial', *Trials,* 21(1), pp. 691.

Winn, M. D., Ballard, C. C., Cowtan, K. D., Dodson, E. J., Emsley, P., Evans, P. R., Keegan, R. M., Krissinel, E. B., Leslie, A. G., McCoy, A., McNicholas, S. J., Murshudov, G. N., Pannu, N. S., Potterton, E. A., Powell, H. R., Read, R. J., Vagin, A. and Wilson, K. S. (2011) 'Overview of the CCP4 suite and current developments', *Acta Crystallogr D Biol Crystallogr,* 67(Pt 4), pp. 235-42.

Wong, W. K., Robinson, S. A., Bujotzek, A., Georges, G., Lewis, A. P., Shi, J., Snowden, J., Taddese, B. and Deane, C. M. (2020) 'Ab-Ligity: Identifying sequence-dissimilar antibodies that bind to the same epitope', *bioRxiv*, pp. 2020.03.24.004051.

Zelek, W. M., Cole, J., Ponsford, M. J., Harrison, R. A., Schroeder, B. E., Webb, N., Jolles, S., Fegan, C., Morgan, M., Wise, M. P. and Morgan, B. P. (2020) 'Complement Inhibition with the C5 Blocker LFG316 in Severe COVID-19', *Am J Respir Crit Care Med*.

Supplementary Material

The allosteric modulation of Complement C5 by knob domain peptides

Alex Macpherson[1,2]*, Maisem Laabei[2], Zainab Ahdash[1], Melissa Graewert[3,4], James R. Birtley[1], Sarah Schulze[1], Susan Crennell[2], Sarah A. Robinson[4], Ben Holmes[1], Vladas Oleinikovas[1], Per H. Nilsson[5,6], James Snowden[1], Victoria Ellis[1], Tom Eirik Mollnes[6,7,8], Charlotte M. Deane[4], Dmitri Svergun[3,4], Alastair D.G. Lawson[1] and Jean van den Elsen[2,9]*

[1] UCB, Slough, UK. SL1 3WE;

[2] Department of Biology and Biochemistry, University of Bath, Bath, UK. BA2 7AX;

[3] European Molecular Biology Laboratory, Hamburg Unit, 22607 Hamburg, Germany;

[4] Department of Statistics, University of Oxford, Oxford, UK;

[5] Department of Chemistry and Biomedicine, Linnaeus University, 391 82 Kalmar, Sweden;

[6] Department of Immunology, Oslo University Hospital, University of Oslo, Oslo, Norway;

[7] Research Laboratory, Bodø Hospital, K.G. Jebsen TREC, University of Tromsø, Tromsø, Norway;

[8] Centre of Molecular Inflammation Research, Norwegian University of Science and Technology, Trondheim, Norway;

[9] Centre for Therapeutic Innovation, University of Bath, Bath, UK. BA2 7AX

*email alex.macpherson@ucb.com and bssjmhve@bath.ac.uk

Supplementary Section 1. Functional assays

Classical pathway C5b deposition ELISA.

Data from *n=3*, unless specified.

Construct	Geomean IC50 (nM)	Range (nM)	Average Emax (%)	Range (%)
K8[a]	9.3	3.0-24.5	68.2	59.5 – 79.56
K57	3.6	2.4 – 7.3	100.6	99.1 – 101.7
K92	ND*	ND*	ND*	ND*
K149	ND*	ND*	ND*	ND*

*ND = Not detected.

[a] Data are an average from *n=6*

Alternative pathway C5b deposition ELISA.

Data from *n=3*, unless specified.

Construct	Geomean IC50 (nM)	Range (nM)	Average Emax (%)	Range (%)
K8 [a]	29.2	25.4 – 34.2	91.8	91.4 – 92.3
K57	30.4	22.7 – 52.1	110.3	97.9 – 134.0
K92[b]	32.4	31.5 - 33.1	62.14	58.0 - 67.7
K149	ND*	ND*	ND*	ND*

*ND = Not detected.

[a] Data are an average from *n=5*

[b] Data are an average from *n=4*

Inhibition of classical pathway mediated C5a release.

Data from *n=3* independent titrations, unless otherwise stated

Construct	Geomean IC50 (nM)	Range (nM)	Average Emax (%)	Range (%)
K8 [a]	9.9	3.9 – 18.7	57.7	51.5 – 73.2
K57	4.0	2.8 - 5.6	98.7	95.9 - 100.6
K92	ND*	ND*	ND*	ND*
K149	ND*	ND*	ND*	ND*

*ND = Not detected.

[a] Data are an average from *n=5*

Inhibition of alternative pathway mediated C5a release.

Data from *n=3*, unless otherwise stated

Construct	Geomean IC50 (nM)	Range (nM)	Average Emax (%)	Range (%)
K8[a]	150.2	49.3 – 85.86	71.8	49.3 – 85.9
K57	26.6	25.0-27.7	97.8	95.1 - 101.3
K92	43.3	39.9 – 45.3	43.3	39.9 – 45.2
K149	ND*	ND*	ND*	ND*

*ND = Not detected.

[a] Data are an average from *n=4*

Inhibition of classical pathway mediated C9 deposition.

Data from *n=3*

Construct	Geomean IC$_{50}$ (nM)	Range (nM)	Average Emax (%)	Range (%)
K8$^{\#}$	-	-	63.4	-
K57	1.9	1.3-2.5	97.9	92.4 - 97 .9
K92	ND*	ND*	ND*	ND*
K149	ND*	ND*	ND*	ND*

*ND = Not detected.

$^{\#}$ Hill slopes < 0.5 IC$_{50}$ values not reported.

Inhibition of alternative pathway mediated C9 deposition.

Data from *n=3*, unless otherwise stated.

Construct	Geomean IC$_{50}$ (nM)	Range (nM)	Average Emax (%)	Range (%)
K8	232.4	131.3 – 521.5	73.3	61.2 – 90.74
K57	24.5	20.6 - 27.6	100.7	100.1 - 100.9
K92	791.9	759.8 - 846.7	44.2	40.9 – 45.9
K149	ND*	ND*	ND*	ND*

*ND = Not detected.

Inhibition of classical pathway haemolysis.

Data from *n=3*

Construct	Geomean IC$_{50}$ (nM)	Range (nM)	Average Emax (%)	Range (%)
K8$^{\#}$	-	-	95.6	91.7 – 99.7
K57	5.3	4.9 – 5.7	99.7	99.2 –100.1
K92	ND*	ND*	ND*	ND*

*ND = Not detected.

$^{\#}$ curves not well described by a 4-PL fit, IC$_{50}$ values not reported.

Inhibition of alternative pathway haemolysis.

Data from *n=3*

| Construct	Geomean IC$_{50}$ (nM)	Range (nM)	Average Emax (%)	Range (%)
K8	ND*	ND*	ND*	ND*
K57	402.7	218 – 660	102.2	90.9 – 109.6
K92	16.9	11.41 – 21.8	31.4	24.1 – 45.3

*ND = Not detected.

Supplementary Section 2. X-ray Crystallography

## Supplementary 2.1 Table of data collection and structure refinement statistics

	C5-K8	C5-K92
Data collection		
Space group	P 21 21 21	C 1 2 1
Cell dimensions		
a, b, c (Å)	81.56, 161.69, 187.38	204.27, 104.29, 154.88
α, β, γ (°)	90, 90, 90	90, 124.89, 90
Resolution (Å)	81.07-2.3 (2.382-2.3)[a]	83.77-2.75 (2.848-2.75)
R_{merge}	0.043 (0.361)	0.018 (0.204)
$I / \sigma I$	13.17 (2.07)	28.79 (4.38)
$CC_{1/2}$	0.99 (0.67)	0.99 (0.92)
Completeness (%)	0.99 (0.99)	0.99 (0.99)
Redundancy	13.5 (13.0)	13.9 (14.0)
Refinement		
Resolution (Å)	81.56-2.3	83.77-2.75
No. reflections	110479 (10914)	69381 (6877)
R_{work} / R_{free}	0.202/0.234	0.219/0.253
No. atoms (non-H)	12100	13095
Protein	11618	13024
Ligand/ion	80	59
Water	402	12
B factors		
Protein	65.4	100.5
Ligand/ion	87.9	122.7
Water	51.9	65.3
r.m.s. deviations		
Bond lengths (Å)	0.003	0.002
Bond angles (°)	0.62	0.58

[a]Values in parentheses are for highest-resolution shell.

Supplementary 2.2. C5-K8 unit cell and crystal packing. A unit cell with a single molecule of the C5-K8 complex is shown followed by orthogonal views showing packing interactions as seen in the crystal lattice. C5-K8 is shown in cartoon representation with C5 coloured blue and K8 in orange. Symmetry-related molecules of C5 are coloured magenta with K8 in orange.
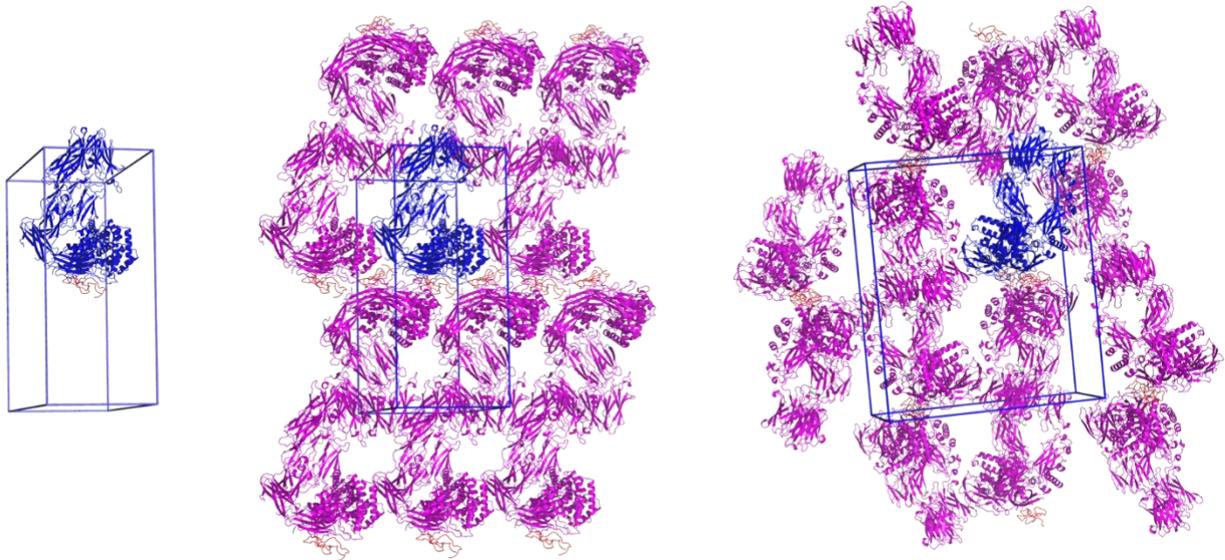

Supplementary 2.3. C5-K92 unit cell and crystal packing. A unit cell with a single molecule of the C5-K92 complex is shown followed by orthogonal views showing packing interactions as seen in the crystal lattice. C5-K92 is shown in cartoon representation with C5 coloured blue and K92 in orange. Symmetry-related molecules of C5 are coloured magenta with K92 in orange**.**
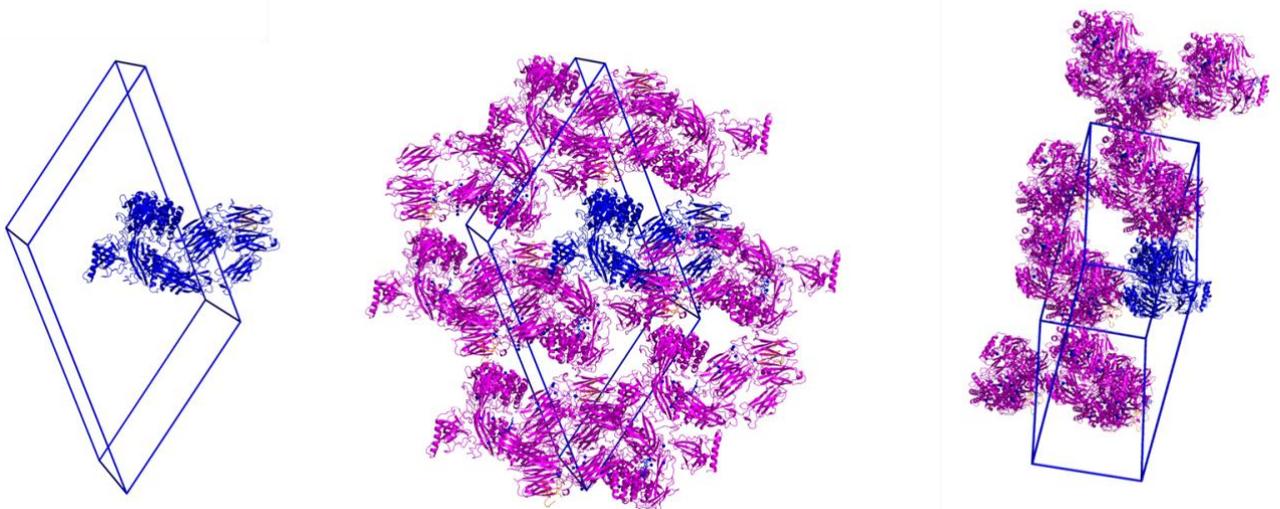
Supplementary figure 2.4. Simulated annealing omit maps of the C5-peptide complexes. The grey mesh shows mFo-DFc simulated annealing omit maps calculated in PHENIX and contoured at a) 3.0 sigma around the K8 peptide and b) at 1.0 sigma around the K92 peptide. In the omit calculation the peptides were deleted from the model. The peptides are displayed in green in cartoon representations with side chains shown as sticks and coloured according to the atom type (nitrogen in blue, oxygen in red, carbon in green and sulphur in yellow). Selected side chains are highlighted.

a)

b)

6
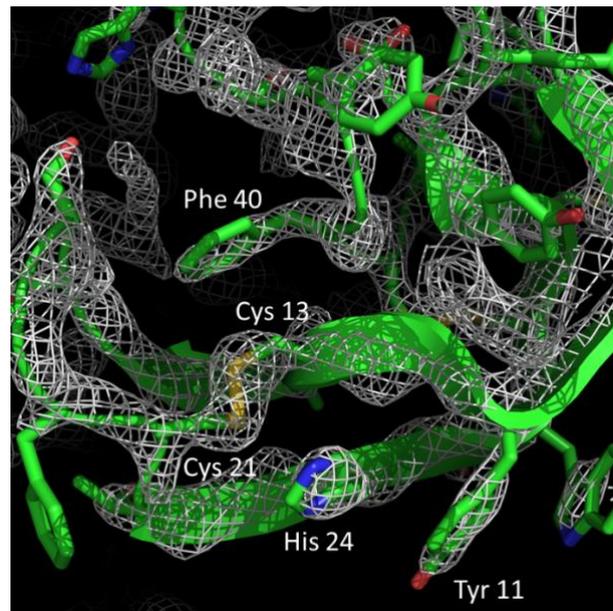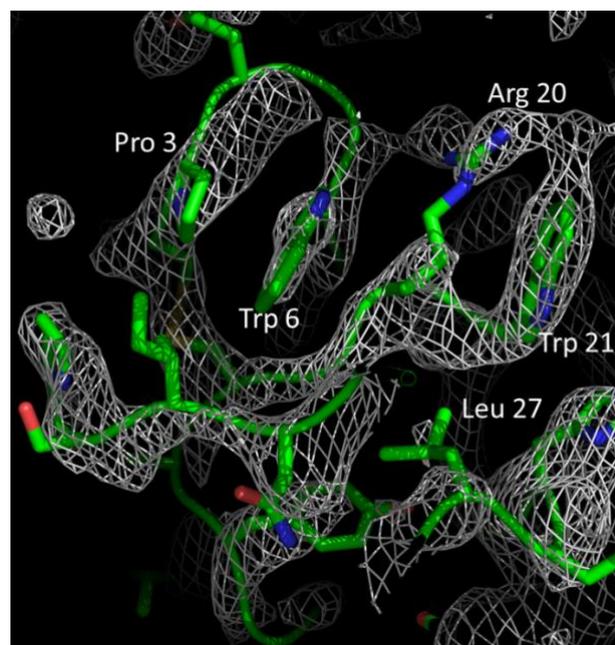
Supplementary 2.5. Structural topology of the K8 peptide.
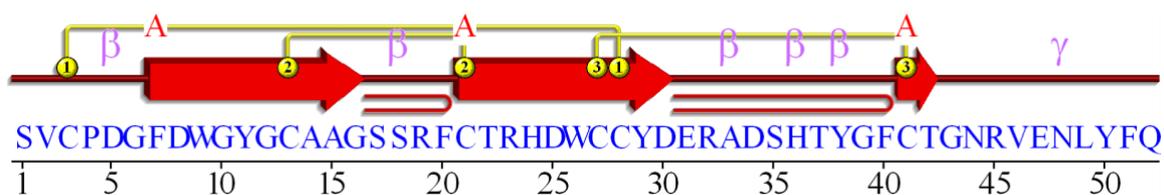
Supplementary 2.6. Table of ionic interactions between K8 and C5. Ionic interactions as defined by the PDBePiSA macromolecular interfaces tool.

K8		C5	
Ionic interactions (5)			
D25	OD2	NZ	K1409
R32	NH1	OD2	D1471
	NH2	OD1/OD2	
H36	NE2	OD1	D1382

Supplementary 2.7 Table of hydrogen bonds between K8 and C5. Hydrogen bonding interactions as defined by the PDBePiSA macromolecular interfaces tool.

K8		C5	
Hydrogen bonds (18)			
A14	O	N	L1379
G16	N	O	L1379
	O	N	I1381
S18	N	OD2	D1382
	OG	NZ	K1380
R23	NH1	O	E1373
		O	S1371
	NH2	O	E1373
D25	OD2	OH	Y1378
	OD2	NZ	K1409
R32	NH1	OD2	D1471
	NH2	OD1	
H36	NE2	OD1	D1382
G43	N	OG	S1407
N44	N	O	S1469
	ND2	O	S1470
R45	NH1	O	S1411
	NH2	O	E1414

7

Supplementary 2.8. Disulphide mapping of the K92 peptide.

Table of intensities and resulting % (by total intensity) for the various peptides linked by a single disulphide bond as identified by Biopharma Finder.

Cysteine Pairing	Intensity[a]	% (by total intensity)
Cys23 to Cys9	150564035	62.71
Cys18 to Cys2	85987873	35.81
Cys23 to Cys2	2796033	1.16
Cys23 to Cys23	527299	0.22
Cys18 to Cys9	166812	0.07
Cys23 to Cys18	17112	0.01
Cys2 to Cys2	15354	0.01
Cys18 to Cys18	11924	0.00
Cys2 to Cys9	5193	0.00

[a] Sum of intensities of all peptides (containing a single disulphide bond) identified by Biopharma Finder as containing the same paired cysteines.

Supplementary 2.9. Structural topology of the K92 peptide.
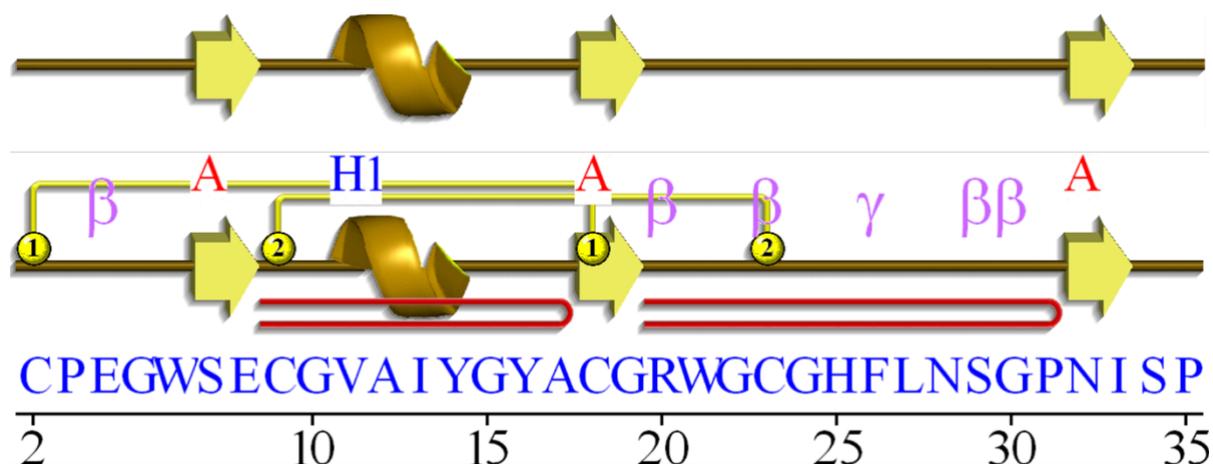
Supplementary 2.10 Table of hydrogen bonds between K92 and C5. Hydrogen bonding interactions as defined by the PDBePiSA macromolecular interfaces tool.

K92		C5	
Hydrogen bonds (8)			
G22	N	OD1	N81
H25	NE2	O	A77
F26	N	O	F512
I13	O	ND2	N533
C23	O	ND2	N38
	O	OG	S82
	N	OG	S82
G24	O	N	F512

9

Supplementary 2.11. Stacking interactions of K92.
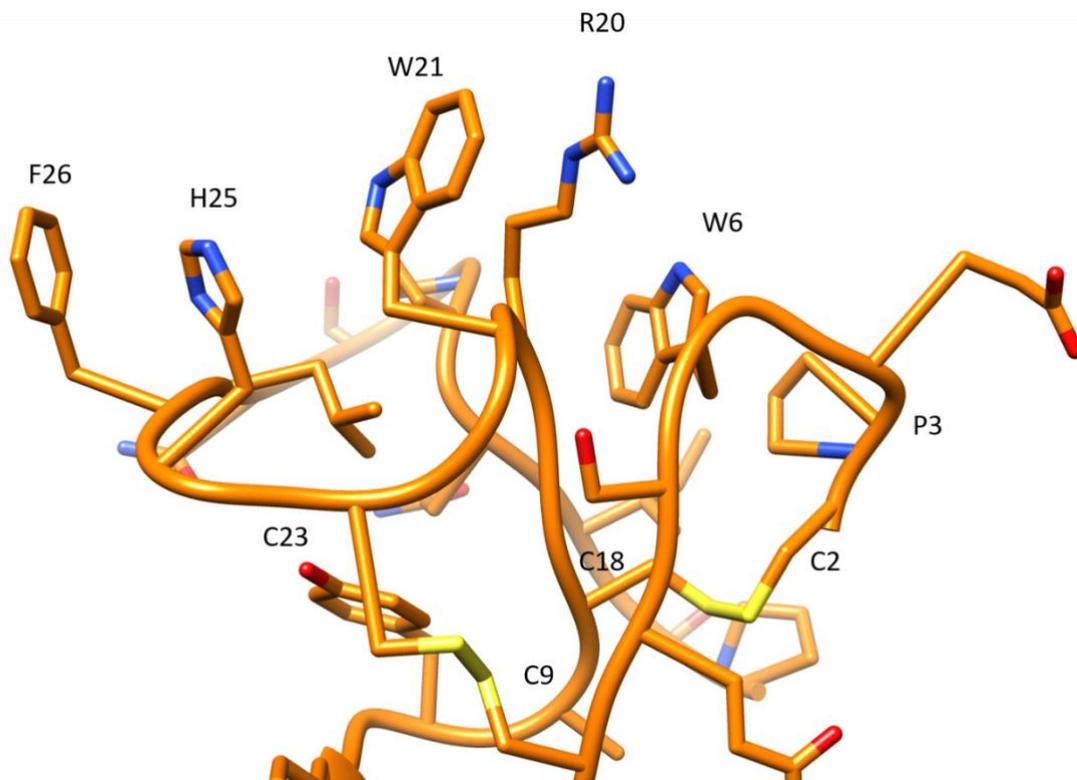
An elegant series of π-π and π-aliphatic stacking interactions mark one face of the K92 peptide. The ordering of F26$_{K92}$-H25 $_{K92}$-W21 $_{K92}$-R20 $_{K92}$-W6 $_{K92}$-P3 $_{K92}$ create a hydrophobic face through which decrease the desolvation entropy for hydrogen bonds made from the polar nitrogen of H25 $_{K92}$ to C5.

Supplementary 2.12. **Individual, total and average hydrogen bond persistence in a binding pose metadynamics simulation of K8-C5**

HBond K8	HBond C5	Persistence score
14:O	1379:H	1.000
16:H	1379:O	0.018
16O	1381:H	1.000
18:H	1382:OD1(OD2)	1.000
23:HH12(HH11,HH21,HH22)	1373:O	0.355
23:HH22(HH11,HH12,HH21)	1373:O	0.355
25:OD2(OD1)	1378:HH	0.964
32:HH12(HH11,HH21,HH22)	1471:OD2(OD1)	0.891
32:HH22(HH11,HH12,HH21)	1471:OD2(OD1)	0.891
43:H	1407:OG	0.609
44:HD22(HD21)	1470:O	0.900
	Total:	7.98
	Average:	0.726

Supplementary 2.13. Individual, total and average hydrogen bond persistence in a binding pose metadynamics simulation of K92-C5

HBond K92	HBond C5	Persistence score
13:O	533:HD21(HD22)	0.909
22:H	81:OD1	0.209
23:O	38:HD22(HD21)	0.536
24:O	512:H	0.536
25:HE2	80:O	0.545
	Total:	2.74
	Average:	0.547

Supplementary 2.14. Paratope size. Comparison of K8 and K92 paratope size to nonredundant antibodies in SAbDab (N= 924). Paratopes were defined as antibody residues within 4.5Å of the antigen in the co-crystal structure.
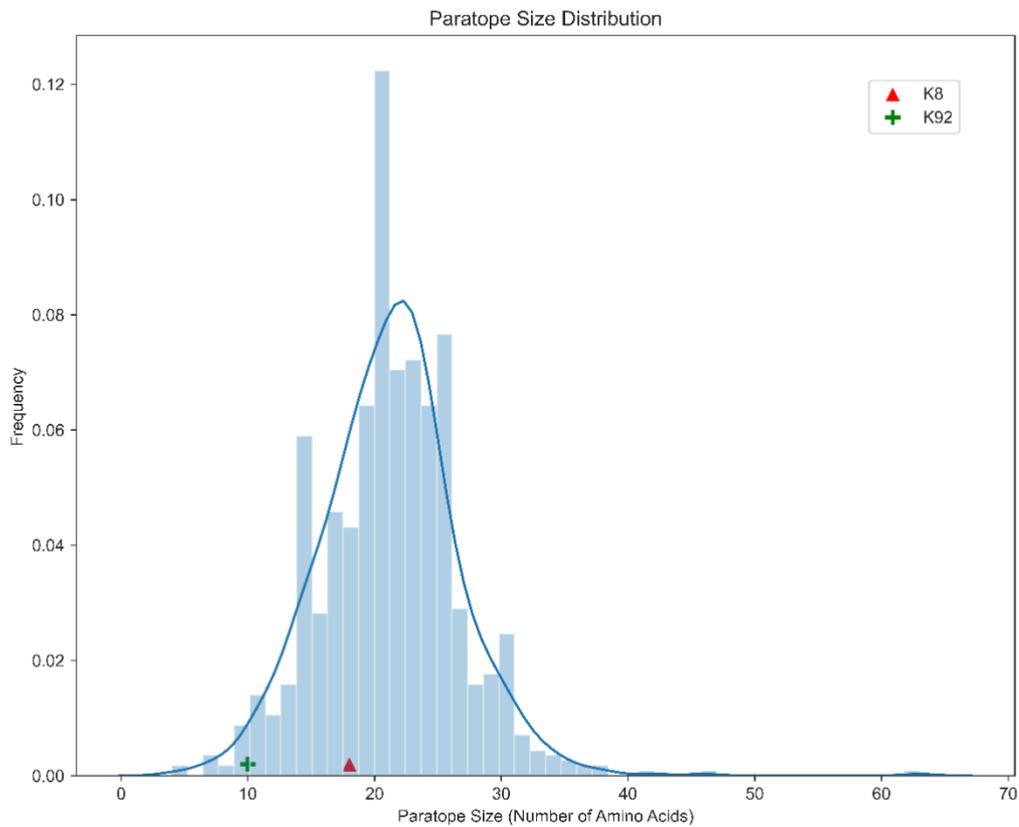
Supplementary 2.15. Amino acid presence in paratope (defined as residues 4.5 Å from C5). Comparison of K8 and K92 paratope composition to nonredundant antibodies in SAbDab (n = 924). Paratopes were defined as antibody residues within 4.5Å of the antigen in the co-crystal structure. Error bars of 1x SD are included for SAbDab dataset.
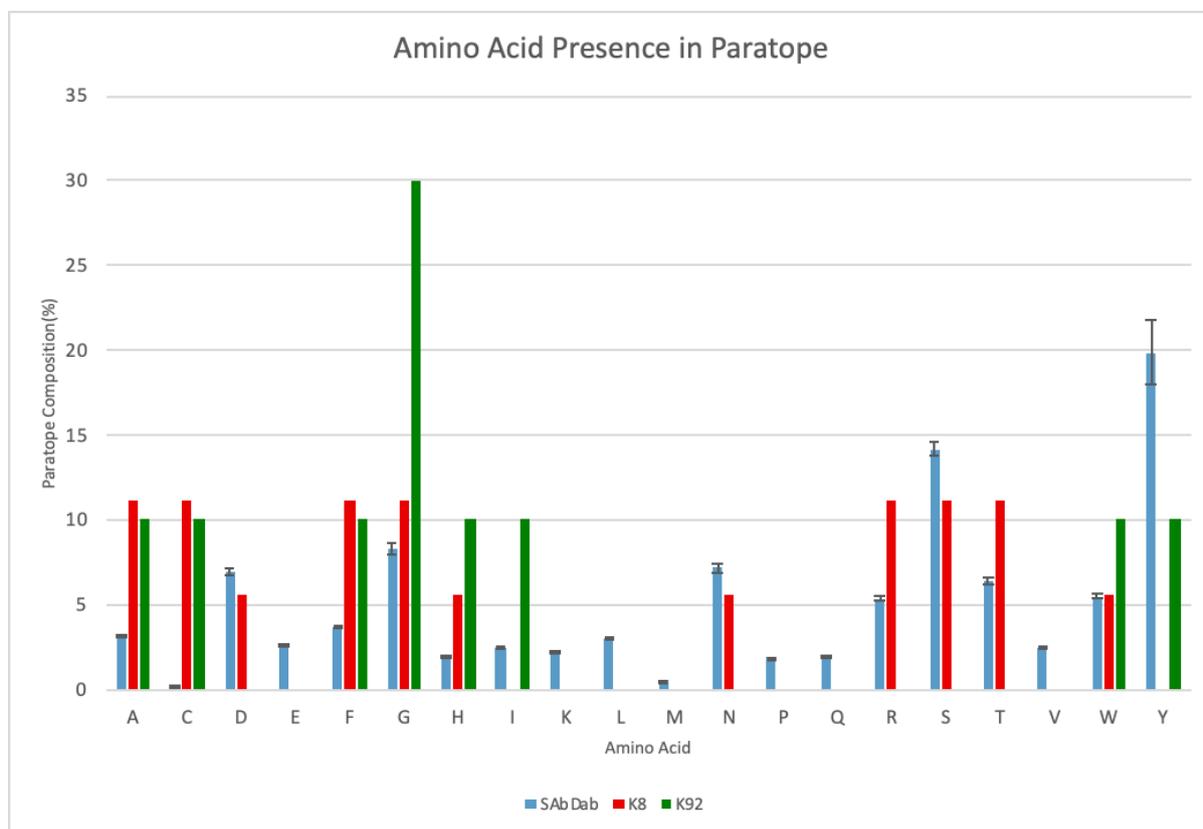
Supplementary Section 3. Small Angle X-ray Scattering

Supplementary 3.1. SAXS Summary Data Table

Data collection parameters	C5	C5-K8	C5-K57	C5-K92	CK-149:
Instrument	EMBL P12 (PETRA III, DESY, Hamburg)				
Beam geometry (mm^2)	0.2×0.12				
Wavelength (nm)	12.4				
s range (nm^{-1})	0.03-7.1				
Temperature (K)	293				
Concentration range (ml)	5.96				
SEC parameters					
Column	Superdex 200 Increase 5/150 column				
Buffer	20mM Tris pH 7.35, 75mM NaCl, and 3% glycerol				
Flow rate, duration	0.35 ml/min; 15 min (900 frames)				
Structural parameters					
R_g (nm) (from $P(r)$)	4.8 ± 0.1	5.4 ± 0.1	5.2 ± 0.1	5.0 ± 0.1	4.9 ± 0.1
R_g (nm) (from Guinier plot)	4.8 ± 0.1	5.4 ± 0.1	5.3 ± 0.1	5.1 ± 0.1	5.0 ± 0.1
D_{max} (nm)	17.6 ± 0.5	18.3 ± 10	19 ± 0.5	19 ± 0.5	18.5 ± 0.5
Porod volume estimate, V_p (nm^3)	390 ± 10	450 ± 10	410 ± 10	410 ± 10	410 ± 10
Molecular weight determination (kDa)					
From volume of correlation, VC	210 ± 20	240 ± 25	230 ± 25	220 ± 22	220 ± 22
From *MALLS*	188 ± 9	200 ± 10	199 ± 10	197 ± 10	195 ± 10
Calculated monomeric *MW* from sequence	186	192	190	191.5	190
Software employed					
Primary data reduction	SASFLOW				
Data processing	CHROMIXS/PRIMUS				
Computation of model intensities	CRYSOL				
normal mode analysis	SREFLEX				

Supplementary 3.2 SEC-MALLS and SEC-SAXS chromatograms for C5-knob domain complexes.

SEC-MALLS chromatograms for C5-knob domain complexes show a homogenous molecular weight increase across the elution peak. The SEC-SAXS elution profile collected under identical experimental conditions shows an increase in radius of gyration (R_G) for the complexes.
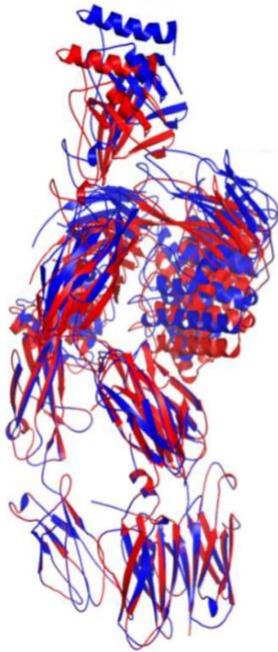

15
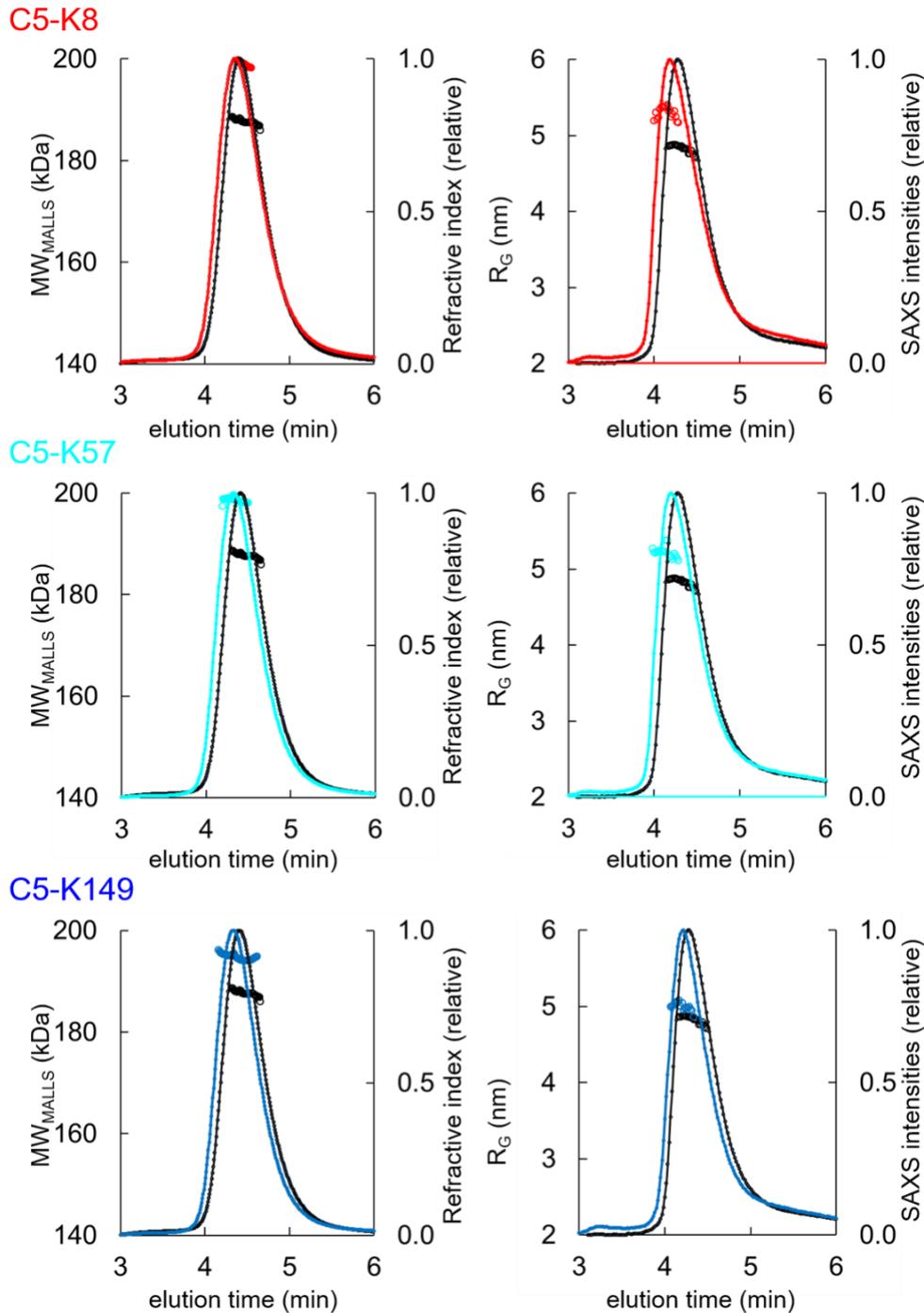
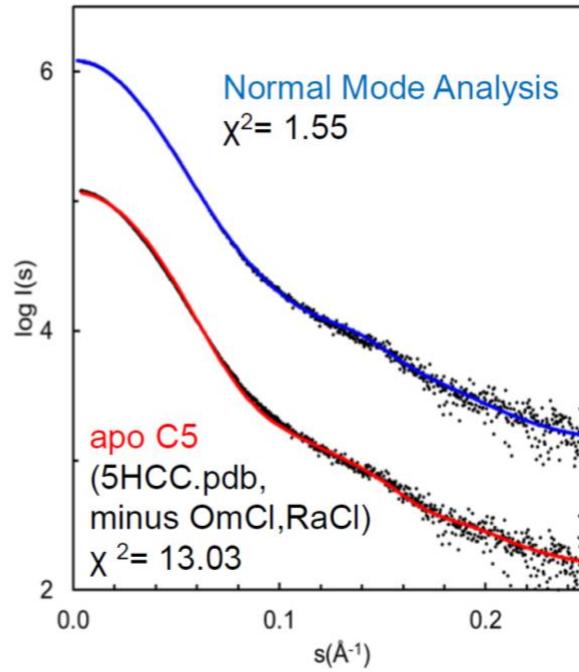**Supplementary 3.3 Solution structure of complement C5 in apo state.**

a) Overlay of cartoon representations of the C5 (red) and the model obtained with SREFLEX (normal mode analysis, blue).

b) Right, the respective fits of the theoretical scattering curves to the SAXS data. χ^2 values are indicated.
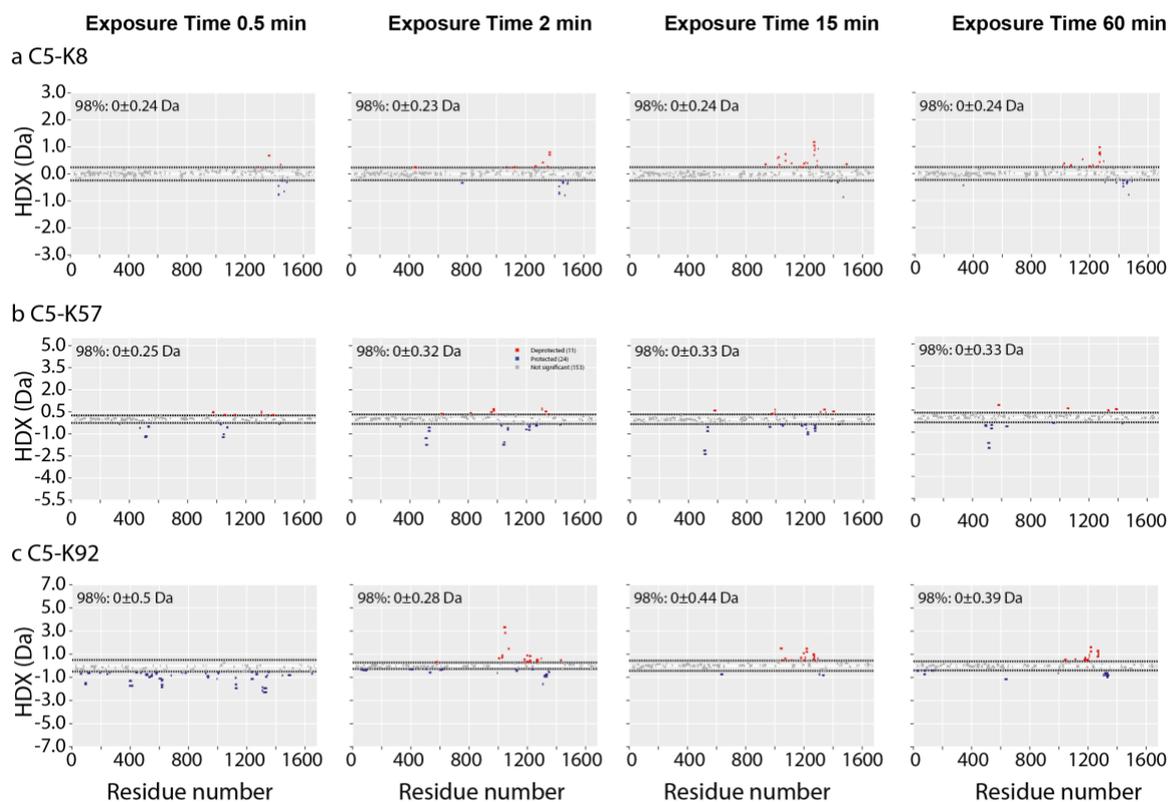
a)   b)

Supplementary Section 4. HDX-MS

Supplementary Figure 4.1 Woods plot displaying the differential HDX (ΔHDX) for C5 in complex with knob domains (a) K8, (b) K57 and (c) K92 at four deterium exposure time points: 0.5 min, 2 min, 15 min and 1 hr. Blue denotes peptides with decreased HDX and red denotes peptides with increased HDX. 98% confidence intervals are shown as dotted lines.

Supplementary Figure 4.2. Linear coverage map for C5 data in complex with knob domains

(a) K8, (b) K57 and (c) K92.
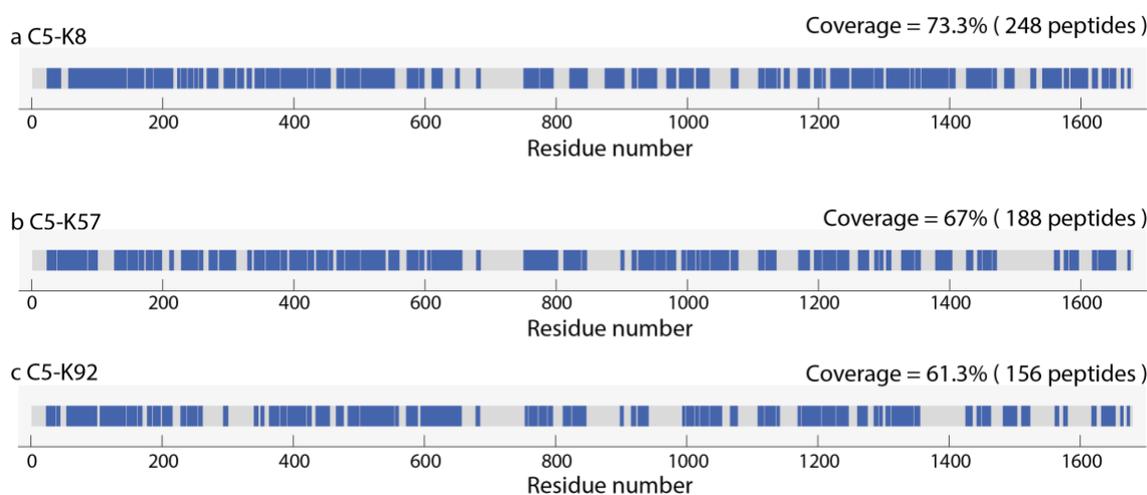
Supplementary Table 4.3. HDX data summary table for ΔHDX of C5 in complex with knob domains K8, K57 and K92.

Data set	ΔHDX = (C5 + K8) − (C5)	ΔHDX = (C5 + K57) − (C5)	ΔHDX = (C5 + K92) − (C5)
Protein buffer conditions	PBS, pH 7.2		
Deuterium time course analysed	30, 120, 900 and 3600 sec		
Number of peptides	248	188	156
Sequence coverage	73.3 %	67.0 %	61.3 %
Redundancy	2.43	2.10	2.43
Replicates	Triplicates		
Average standard deviation	0.06	0.08	0.09
Significant differences at 1 hour ΔHDX*	CI 98% = 0± 24 Da	CI 98% = 0± 33 Da	CI 98% = 0± 39 Da

* To compare significant differences, a T-test with α=0.02 was used. Only peptides which satisfied a ΔHDX confidence interval of 98 % were considered significant.

Supplementary 5.1 SPR single-cycle kinetics of knob domains binding to human C5b

Data Table (summary of *n=3*)

	Chi² (RU²)	mean k_{on} (1/Ms)	mean k_{off} (1/s)	mean K_D (M)	Mean stoichiometric ratio	comment
K8	-	-	-	-	0.1	Non-binding
K92	0.04	1.14E+05	6.20E-05	5.48E-10	0.4	
K57	0.07	2.51E+05	3.54E-04	1.41E-09	0.4	
K149	0.03	7.49E+05	3.76E-03	5.02E-09	0.4	

n=1

	Chi² (RU²)	k_{on} (1/Ms)	k_{off} (1/s)	K_D (M)	Rmax (RU)	Stoichiometric ratio	comment
K8	-	-	-	-	2.1	0.1	Non-binding
K92	0.06	1.11E+05	5.20E-05	4.67E-10	5.4	0.4	
K57	0.05	2.73E+05	3.75E-04	1.37E-09	6.2	0.4	
K149	0.03	7.56E+05	3.65E-03	4.83E-09	2.8	0.3	

n=2

	Chi² (RU²)	k_{on} (1/Ms)	k_{off} (1/s)	K_D (M)	Rmax (RU)	Stoichiometric ratio	comment
K8	-	-	-	-	2.4	0.1	Non-binding
K92	0.03	1.10E+05	7.68E-05	6.99E-10	5.2	0.4	
K57	0.08	2.40E+05	3.46E-04	1.44E-09	8.2	0.4	
k149	0.03	7.80E+05	3.99E-03	5.11E-09	5.1	0.4	

n=3

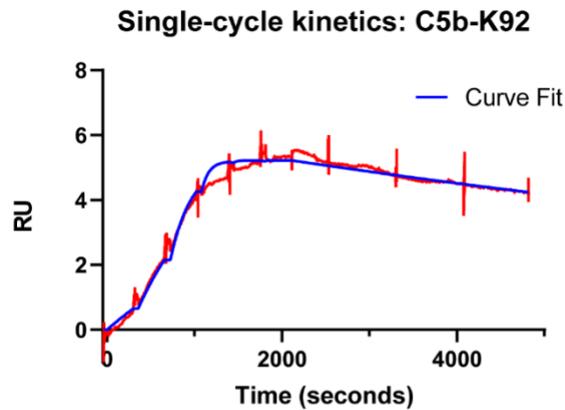|	Chi² (RU²)	k_{on} (1/Ms)	k_{off} (1/s)	K_D (M)	Rmax (RU)	Stoichiometric ratio	comment
K8	-	-	-	-	2.6	0.2	Non-binding
K92	0.03	1.20E+05	5.73E-05	4.78E-10	4.7	0.3	
K57	0.08	2.38E+05	3.42E-04	1.43E-09	7.9	0.4	
K149	0.03	7.12E+05	3.65E-03	5.13E-09	5.2	0.4	

Supplementary Figure 5.2 SPR single-cycle kinetics of knob domains binding to human C5b. Example sensorgrams and curve fits (1:1 binding model) are shown with summary kinetics from *n=3* experiments.
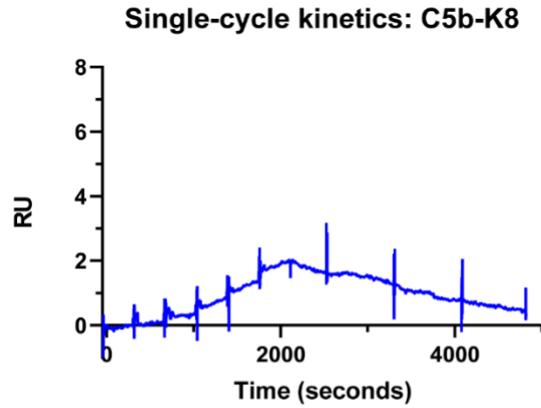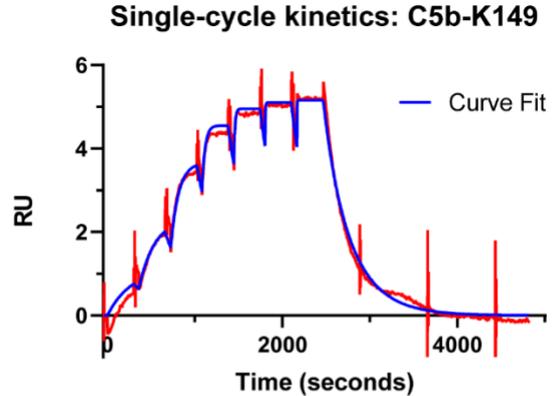

Single-cycle kinetics: C5b-K8
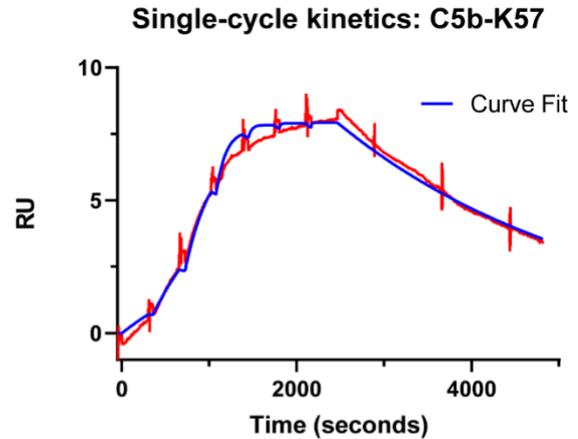
Stoichiometric ratio at 1µM = 0.1
Non-binding

Single-cycle kinetics: C5b-K57

mean k_{on} = 2.51 x10^5 1/Ms
mean k_{off} = 3.54 x10^{-4} 1/s
mean K_D = 1.41 x10^{-9} M
mean stoichiometric ratio at 1 µM = 0.4

Single-cycle kinetics: C5b-K92

mean k_{on} = 1.14 x10^5 1/Ms
mean k_{off} = 6.20 x10^{-5} 1/s
mean K_D = 5.48 x10^{-10} M
mean stoichiometric ratio at 1 µM = 0.4

Single-cycle kinetics: C5b-K149

mean k_{on} = 7.49 x10^5 1/Ms
mean k_{off} = 3.76 x10^{-3} 1/s
mean K_D = 5.02 x10^{-9} M
mean stoichiometric ratio at 1 µM = 0.4

20